Petroleum Science 23 (2026) 4873–4890

Contents lists available at ScienceDirect

Petroleum Science

journal homepage: www.keaipublishing.com/en/journals/petroleum-science

Original Paper

Energy-efficient fracturing based on stress-coupled perforation

Cheng Cheng [a], Gang Hui [a,b,*], Zhang-Xin Chen [c,b,**]

[a] State Key Laboratory of Oil and Gas Reservoir Geology and Exploitation, Chengdu University of Technology, Chengdu, 610059, SiChuan, China
[b] State Key Laboratory of Petroleum Resources and Engineering, China University of Petroleum (Beijing), Beijing, 102249, China
[c] Ningbo Key Laboratory of Low-Carbon Hydrogen Energy, Eastern Institute of Technology, Ningbo, 315200, Zhejiang, China

ARTICLE INFO

Article history:
Received 28 August 2025
Received in revised form
15 January 2026
Accepted 27 March 2026
Available online 1 April 2026

Edited by Xi Zhang

Keywords:
Multi-stage fracturing
Stress-coupled perforation
Dynamic stress distribution
Multi-fracture growth
Energy consumption

ABSTRACT

Hydraulic fracturing (HF) in horizontal wells frequently encounters challenges such as uneven fracture propagation and elevated energy consumption, largely due to stress shadow effects and perforation inefficiencies. This paper presents a novel stress-coupled perforation (SCP) technique that dynamically optimizes perforation cluster parameters by integrating real-time stress interference. The approach employs a semi-numerical model grounded in linear elastic fracture mechanics (LEFM) and energy conservation principles, enabling rapid simulation of multi-fracture propagation with high accuracy. Field applications in both homogeneous and heterogeneous shale reservoirs demonstrate that SCP achieves more uniform fracture development while reducing energy consumption by 22%–37% per unit fracture area compared to the conventional extreme limited entry (EXL) method, without sacrificing fracture coverage. The method offers a practical and sustainable pathway to improve HF efficiency, lower operational costs, and reduce environmental impact.

1. Introduction

Hydraulic fracturing (HF) serves as a cornerstone technology for the development of low-permeability and unconventional hydrocarbon reservoirs. The process involves injecting fluid at high pressure through multiple perforation clusters (typically 3–6) within a horizontal wellbore to create fractures, which are then propped open to facilitate hydrocarbon flow. However, field diagnostics consistently indicate that 20% to 40% of perforation clusters contribute negligibly to production, highlighting the persistent challenge of non-uniform fracture growth (Miller et al., 2011; Hui et al., 2023a; Baihly et al., 2010). This unevenness is not a result of independent fracture propagation but arises from a complex, coupled competitive system (Bunger and Peirce, 2014; Hui et al., 2023b; Cornelius et al., 2018; Meyer and Bazan, 2011).

The propagation patterns and interactions within a cluster of simultaneously growing fractures are governed by several interlinked mechanisms. First, the multi-fracture propagation pattern is inherently competitive. Fully coupled 3D simulations demonstrate that the number of fractures that can sustain effective growth is limited by geometric constraints (e.g., height confinement, cluster spacing) and the dominance of viscous dissipation, often leading to localization where only a subset of fractures propagates significantly (Bunger and Peirce, 2014; Hui et al., 2024, 2025; Bao et al., 2025; Rijeka, 2016). A common pattern is the preferential growth of edge fractures while interior fractures are suppressed. Second, this competition is driven by fracture-fracture interaction mechanisms, which include: (i) Elastic coupling (stress shadowing), where an opening fracture induces a stress increase in the surrounding rock, elevating the minimum principal stress near neighboring fractures and hindering their initiation and growth (Abass et al., 2009; Fisher et al., 2004; Taghichian et al., 2014; Wang et al., 2023; Wu et al., 2025). (ii) Hydraulic coupling, involving the dynamic redistribution of injected fluid among clusters. A slight initial advantage in one fracture can create a positive feedback loop—increased net pressure and aperture strengthen its stress shadow, which further attracts more fluid flow, exacerbating growth non-uniformity. (iii) Near-wellbore and time-sequence effects, such as perforation entry friction, tortuosity, asynchronous initiation, and perforation erosion, which dynamically alter the effective boundary conditions for each cluster (Bunger and Lecampion, 2017).

* Corresponding author.
** Corresponding author.
E-mail addresses: hui.gang@cup.edu.cn (G. Hui), zhachen@ucalgary.ca (Z.-X. Chen).
Peer review under the responsibility of China University of Petroleum (Beijing).

https://doi.org/10.1016/j.petsci.2026.03.063

Despite substantial progress in understanding these mechanisms, significant gaps remain in translating this knowledge into predictive and optimized engineering design. Key limitations of existing studies include: incomplete coupling dimensions, where the closed-loop feedback among stress shadowing, flow partitioning, and near-wellbore effects is not fully captured within a unified framework (Bunger and Lecampion, 2017; Scanlon et al., 2014); insufficient realism of engineering boundary conditions, often overlooking practical complexities like time-varying perforation erosion and initiation asynchrony (Dontsov et al., 2023); limited representativeness of parameter space relative to modern high-cluster-count designs; and challenges in model verification due to insufficient field monitoring constraints. These gaps hinder the development of robust design strategies to improve cluster efficiency.

To mitigate growth non-uniformity, the industry widely employs the extremely limited entry (EXL) perforation technique. It aims to control fluid distribution by creating high perforation friction. However, if applied without accounting for dynamic stress and propagation behavior, the required perforation pressure drop can be several times the fracturing pressure (Howard and Fast, 1970; Lecampion and Desroches, 2015). This necessitates a significant increase in pumping pressure and power to maintain injection rates (Hui et al., 2021), elevating operational costs—fracturing pumping can account for approximately 41% of total well investment (Kondash et al., 2018). Consequently, the EXL technique exacerbates environmental concerns, including higher greenhouse gas emissions, water resource management challenges, induced seismicity risks, and resource waste (Ellsworth, 2013; Entrekin et al., 2018; Vengosh et al., 2014; Cheng, 2021; Mitchell et al., 2013). These negative impacts are intrinsically linked to increased energy expenditure. Thus, a dual imperative exists: enhancing fracture growth uniformity while drastically reducing the energy intensity and environmental footprint of completions (Laurenzi and Jersey, 2013; Vafi and Brandt, 2016).

To address these intertwined challenges, this paper proposes a novel SCP technique. The SCP technique strategically manages fracture competition by accounting for dynamic inter- and intra-stage stress interference, explicitly optimizing the trade-off between fracture development and energy consumption. In contrast to the conventional EXL approach characterized by substantial pressure-drop losses, SCP deliberately accepts a marginal reduction in total fracture area in exchange for a significant reduction in energy input. Numerical experiments demonstrate that SCP can achieve energy savings of approximately 20% in homogeneous reservoirs with only a minor decrease in fracture area. This efficiency advantage is more pronounced in heterogeneous reservoirs (e.g., multi-well pad developments), where energy savings of up to about 37% can be realized while maintaining a comparable fracture area, thereby reducing both cost and carbon emissions. This paper first presents a mathematical model for fracture propagation based on linear elastic fracture mechanics, then describes the computational algorithm and numerical experiments, followed by the presentation of key findings and concluding remarks.

2. Methods

2.1. Calculation method for dynamic stress distribution

Stage fracturing is a dynamic process in which the stress undergoes variation in the surrounding medium of operation wellbore. The SCP technique is the optimal combination of perforation hole count and hole diameter, based on the accurate prediction of dynamic stress distribution.

To precisely calculate its numerical value, each fracture corresponding to a perforation cluster is first written in the form of $F_{i,j,k}$. Here, i refers to the i-th well in the well group, j refers to the j-th stage in the well respectively, and k denotes the k-th fracture within a stage, with $k = 1$ near the toe and $k = 5$ near the heel (Fig. 1). Once each fracture is marked, the normal stress at any point in space can be calculated according to the elastic stress equation. Assuming an arbitrary point C in the reservoir with a horizontal coordinate of x, a vertical coordinate of y, and a height coordinate of z, the method for calculating the normal stress in point C due to deformation of fracture $F_{i,j,k}$ is illustrated as follows: the fracture $F_{i,j,k}$ corresponds to the spatial position A of the perforation cluster $\left(x_{i,j,k},\ y_{i,j,k},\ z_{i,j,k}\right)$, and the fracture $F_{i,j,k+1}$ corresponds to the spatial position B of the perforation cluster $\left(x_{i,j,k+1},\ y_{i,j,k+1},\ z_{i,j,k+1}\right)$. The corresponding position vectors can then be written as $\overrightarrow{AC} = \left(x - x_{i,j,k}, y - y_{i,j,k}, z - z_{i,j,k}\right)$ and $\overrightarrow{AB} = \left(x_{i,j,k-1} - x_{i,j,k}, y_{i,j,k-1} - y_{i,j,k}, z_{i,j,k-1} - z_{i,j,k}\right)$. The projection length of vector $\overrightarrow{AC}$ on vector $\overrightarrow{AB}$ is given by $(\overrightarrow{AC} \cdot \overrightarrow{AB})/|\overrightarrow{AB}|$, where $|\overrightarrow{AB}|$ denotes the modulus of vector $\overrightarrow{AB}$, that is, the length from point A to point B. Then, using the Pythagorean theorem, the vertical distance D_C from any point C to the plane perpendicular to the well trajectory passing through the perforation cluster $\left(x_{i,j,k},\ y_{i,j,k},\ z_{i,j,k}\right)$ can be obtained through:

$$D_{C,(i,j,k)} = \sqrt{\left|\overrightarrow{AC}\right|^2 - \left[\left(\overrightarrow{AC} \cdot \overrightarrow{AB}\right) \Big/ \left|\overrightarrow{AB}\right|\right]^2} \tag{1}$$

Here, $|\overrightarrow{AC}|$ represents the modulus of vector $|\overrightarrow{AC}|$, which is the distance from point C to point A. The distance from the projection points of any point C in space on the fracture surface $F_{i,j,k}$ to the position $\left(x_{i,j,k},\ y_{i,j,k},\ z_{i,j,k}\right)$ of the corresponding perforation cluster is calculated as:

$$L_{C,(i,j,k)} = \sqrt{\left|\overrightarrow{AC}\right|^2 - \left[D_{C,(i,j,k)}\right]^2} \tag{2}$$

Let:

$$\zeta_{C,(i,j,k)} = \frac{D_{C,(i,j,k)}}{R_{i,j,k}} \rho_{C,(i,j,k)} = \frac{L_{C,(i,j,k)}}{R_{i,j,k}} \tag{3}$$

$\zeta_{C,(i,j,k)}$ is the ratio of the projection vertical distance $D_{C,(i,j,k)}$ to the radius of the fracture $R_{i,j,k}$. As the fracture expands, $R_{i,j,k}$ increases, and the value of $\zeta_{C,(i,j,k)}$ decreases. $\rho_{C,(i,j,k)}$ is the ratio of the distance $L_{C,(i,j,k)}$ between the projection point of point C on the

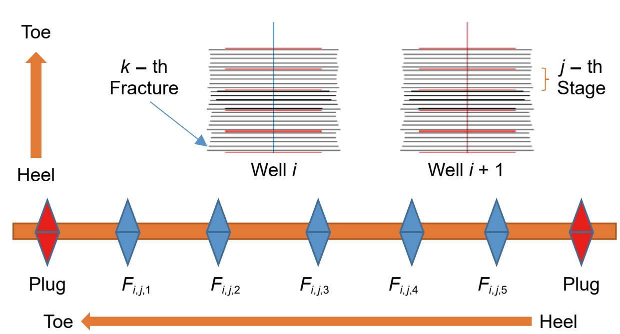

Fig. 1. Schematic diagram of perforation cluster calibration.

fracture surface and the center of the fracture $F_{i,j,k}$ to the fracture radius $R_{i,j,k}$.

$$P_{i,j,k} = \frac{3E'V_{i,j,k}}{16{R_{i,j,k}}^3} \tag{4}$$

$P_{i,j,k}$ is the modified uniform internal net pressure generated by the uniformly pressurized ellipsoidal fracture. Considering that the full elastic solution of each non-uniform and transient internal fracture pressure is the main computational bottleneck. To calculate quickly, Cheng and Bunger (2016) proposed an approximation in which the non-uniform pressure is replaced by uniform pressure, and at each time step, this uniform pressure is chosen to produce a fracture with the same volume as the actual fracture opened by non-uniform internal pressure, that is:

$$V_{i,j,k} = 2\pi \int_0^{R_{i,j,k}(t)} w_{i,j,k}(r,t)\mathrm{d}r \tag{5}$$

Based on the above parameters, according to Eqs. (1)–(5), the normal stress component applied by the fracture $F_{i,j,k}$ to any point C in space is approximately given by:

$$\sigma_{\mathrm{C},(i,j,k)} = \frac{2P_{i,j,k}}{\pi}\left\{\begin{matrix} \delta_{\mathrm{C},(i,j,k)}^{-\frac{1}{2}}\cos\frac{1}{2}\phi_{\mathrm{C},(i,j,k)} - tan^{-1} \\ \dfrac{\left[\begin{matrix}\delta_{\mathrm{C},(i,j,k)}^{\frac{1}{2}}\sin\frac{1}{2}\phi_{\mathrm{C},(i,j,k)} \\ +\tau_{\mathrm{C},(i,j,k)}\sin\theta_{\mathrm{C},(i,j,k)}\end{matrix}\right]}{\left[\begin{matrix}\delta_{\mathrm{C},(i,j,k)}^{\frac{1}{2}}\cos\frac{1}{2}\phi_{\mathrm{C},(i,j,k)} \\ +\tau_{\mathrm{C},(i,j,k)}\cos\theta_{\mathrm{C},(i,j,k)}\end{matrix}\right]} \\ +\zeta_{\mathrm{C},(i,j,k)}\delta_{\mathrm{C},(i,j,k)}^{-\frac{3}{2}} \\ \cos\left(\frac{3}{2}\phi_{\mathrm{C},(i,j,k)} - \theta_{\mathrm{C},(i,j,k)}\right) \\ -\zeta_{\mathrm{C},(i,j,k)}\delta_{\mathrm{C},(i,j,k)}^{-\frac{1}{2}}\sin\frac{1}{2}\phi_{\mathrm{C},(i,j,k)} \end{matrix}\right\} \tag{6}$$

Here, other variables are formed by the fracture length $R_{i,j,k}$ of fracture $F_{i,j,k}$ and Eqs. (7)–(10).

$$\tau_{\mathrm{C},(i,j,k)} = \left(1+\zeta_{\mathrm{C},(i,j,k)}^2\right)^{\frac{1}{2}} \tag{7}$$

$$\theta_{\mathrm{C},(i,j,k)} = \arctan\left(\frac{1}{\zeta_{\mathrm{C},(i,j,k)}}\right) \tag{8}$$

$$\delta_{\mathrm{C},(i,j,k)} = \left\{\begin{matrix}\left[\left(\rho_{\mathrm{C},(i,j,k)}\dfrac{R_{i,j,k}}{L_{\mathrm{C},(i,j,k)}}\right)^2 + \zeta_{\mathrm{C},(i,j,k)}^2 - 1\right]^2 \\ +4\zeta_{\mathrm{C},(i,j,k)}^2\end{matrix}\right\}^{\frac{1}{2}} \tag{9}$$

$$\phi_{\mathrm{C},(i,j,k)} = \mathrm{arccot}\left\{\begin{matrix}\left[\left(\rho_{\mathrm{C},(i,j,k)}\dfrac{R_{i,j,k}}{L_{\mathrm{C},(i,j,k)}}\right)^2 + \zeta_{\mathrm{C},(i,j,k)}^2 - 1\right] \\ \Big/ 2\zeta_{\mathrm{C},(i,j,k)}\end{matrix}\right\} \tag{10}$$

Considering the deformation caused by fracturing during the HF process of a well factory, which exists between wells, stages and clusters, these deformations subsequently change the stress distribution in the formation. As stage fracturing is a dynamic process, the magnitude of stress at any point C in space is a result of stress accumulation, as shown below:

$$\sigma_{\mathrm{C}} = \sum_i^N \sum_j^{n_i} \sum_k^{m_j} \sigma\left(\zeta_{\mathrm{C},(i,j,k)}, \rho_{\mathrm{C},(i,j,k)}, t\right) \tag{11}$$

where N is the number of wells in the well group that have undergone HF, n_i is the number of stages that have been fractured in the i-th well, and m_j is the total number of fractures that are simultaneously fractured in the j-th stage. To calculate the stress distribution of the surrounding rock of the operation well group, just replace the coordinates of point C in above Eq. (11) with the coordinates of the fracture surface, and then the magnitude of the normal stress applied on any fracture can be obtained.

2.2. Calculation method of fracture propagation

During the process of stage fracturing, multiple perforation clusters need to be set up initially in the operation part of the wells (Long and Xu, 2017; Wei et al., 2025; Weng, 1993). Then high-pressure fracturing fluid is injected simultaneously into each perforation cluster. Based on the propagation conditions of LEFM, when the fracture criterion given by Rice (1968) $K_{\mathrm{I}} = K_{\mathrm{IC}}$ is met, the reservoir will be fractured in the direction perpendicular to the minimum in-situ confining stress $\sigma_{\min}$, thus creating a fracture. K_{I} represents the stress intensity factor of Mode I (opening mode), and K_{IC} represents the fracture toughness of Mode I fracture (Rice, 1968).

Fractures must overcome the stress imposed by the surrounding rock in order to propagate. The stress σ_{C} acting on the fracture surface is calculated using Eq. (4). Using the fracture propagation energy calculation formula, we can determine the energy W_{I} consumed by the fracture in overcoming the stress during the propagation process. Taking the fracture $F_{i,j,k+1}$ as an example, the work done to overcome the compressive stress from fracture $F_{i,j,k}$ in its expansion is calculated as:

$$\dot{W}_{\mathrm{I}(i,j,k+1)} = -2\pi\left(\begin{matrix}\displaystyle\int_{R_w}^{\min\left(R_{i,j,k},\ R_{i,j,k+1}\right)} \sigma_{i,j,k}\frac{\partial w_{i,j,k+1}}{\partial t}r\mathrm{d}r \\ +\sigma_{i,j,k}\dfrac{\mathrm{d}R_{i,j,k}}{\mathrm{d}t}R_{i,j,k}w_{i,j,k+1}\left(\dfrac{R_{i,j,k}}{R_{i,j,k+1}}\right)\end{matrix}\right) \tag{12}$$

In addition to overcoming the stress exerted by adjacent and simultaneously fractured fractures, the fracture also needs to overcome the stress induced by the previously cracked fractures. Its power is calculated by the following formula:

$$\dot{W}_{i,j,k} = Q_{i,j,k} \times$$

$$\int_{z_0}^{z_t}\int_{y_0}^{y_t}\int_{x_0}^{x_t}\sum_{i}^{N}\sum_{j}^{n_i}\sum_{k}^{m_j}\sigma_{C,(i,j,k)}(x,y,z,t)\mathrm{d}x\mathrm{d}y\mathrm{d}z \tag{13}$$

The upper and lower limits of the integral in Eq. (13) are determined by the boundaries of the fracture in three-dimensional space. By introducing the work rate $\dot{W}_{\mathrm{f}}$, which represents the power required for a fracture to overcome stress-shadow effects, into the right-hand side of the power-balance equation of Cheng and Bunger (2019c), the influence of stress distribution on flow-rate allocation can be quantified

$$p_{\mathrm{fo}}Q_{i,j,k} = \dot{W}_{\mathrm{C}} + D_{\mathrm{f}} \tag{14}$$

Here, $p_{\mathrm{fo}}Q_{i,j,k}$ represents the total input power (product of pressure and injection flow rate) of the k-th fracture in the j-th stage of the i-th well. $\dot{W}_{\mathrm{C}}$ represents the power consumed by the fluid applied on the solid, mainly including: the rate of work done by the compressive stress induced by fracture i on other fractures W_{I}; the strain energy rate generated by rock deformation U; the work done by the fracture to overcome the minimum in-situ stress $\sigma_{\min}\times Q_{i,j,k}$; the power consumed by the fracture to overcome the stress of already fractured fractures $\dot{W}_{i,j,k}$; and the energy dissipation rate related to rock breakage F_{C}:

$$\dot{W}_{\mathrm{C}} = W_{\mathrm{I}} + U + \sigma_{\min}Q_{i,j,k} + \dot{W}_{i,j,k} + F_{\mathrm{C}} \tag{15}$$

The term D_{f} represents the input power consumed by fluid flow, which are the energy dissipation rate related to viscous fluid flow, F_{f}, the energy loss rate related to fluid leakoff into surrounding rock D_{L}, and the power loss of fracturing fluid flowing through perforation holes into formation P_{perf}:

$$D_{\mathrm{f}} = F_{\mathrm{f}} + D_{\mathrm{L}} + P_{\mathrm{perf}} \tag{16}$$

For detailed explanations of these energy loss rate terms, please refer to the research results published by Cheng and Bunger (2016). Further explanation is not provided here. The energy consuming rate related to perforations, P_{perf}, is expressed by the formula given by Bunger et al. (2014):

$$P_{\mathrm{perf}(i,j,k)} = \left(a\rho \middle/ n_{i,j,k}^2 D_{p(i,j,k)}^4 \mathrm{K}^2\right) Q_{i,j,k}(t)^3 \tag{17}$$

$P_{\mathrm{perf}(i,j,k)}$ is the energy loss at the entrance of fracture k when the fluid passes through, which needs to analyze the pressure drop when the fluid passes through the cluster of $n_{i,j,k}$ perforation holes (Crump and Conway, 1988; Economides and Nolte, 2000). $Q_{i,j,k}(t)$ is the volumetric flow rate through the k-th perforation cluster at time t, which varies with the pumping time t. $n_{i,j,k}$ is the number of perforation holes in the k-th cluster, usually between 5 and 20. $D_{p(i,j,k)}$ represents the perforation diameter of the k-th cluster, generally between 6 and 15 mm. In addition, the perforation hole itself has a shape factor K, which is 0.56 before erosion and 0.89 after erosion (Crump and Conway, 1988). C5Frac neglects hole erosion, so K is 0.56. The numerical factor a often takes the value of 0.8106. The density of the fluid injected into the reservoir is ρ. The variables in the equation brackets form the ratio of power loss passing through the perforation hole. The energy loss of the fluid at the hole is negatively proportional to the fourth power of the hole diameter and the second power of the number of holes. These slight changes in two perforation parameters will have a huge impact on the energy loss of the fluid passing through the hole, thereby directly affecting the fluid distribution between the perforation clusters under the constraint of power balance (Eq. (14)). These two parameters can be manually controlled and adjusted during the completion stage of fracturing, therefore, as the main parameters affecting the fracturing effect and energy consumption, the number of perforation holes and the hole diameter in a single cluster need to be optimized.

The real-time fluid flow rate $Q_{i,j,k}$ for each perforation cluster in the operating section is assumed based on the approximate solution for fracture length, opening, and flow pressure. The traction force quantifying the effect of inter-well, inter-stage, and inter-cluster stress received by the fracture $F_{i,j,k}$ is:

$$T_{i,j,k}\left(\rho_{i,j,k},\mu_{i,j,k}^{c}(t),\psi_{i,j,k}(t)\right) = \left(\frac{E^2\mu_{i,j,k}^{c}(t)}{t}\right)^{\frac{1}{3}}\left\{\begin{array}{c} A\left[\omega-\dfrac{2}{3\left(1-\rho_{i,j,k}\right)^{\frac{1}{3}}}\right] \\ -B\left(\ln\dfrac{\rho_{i,j,k}}{2}+1\right) \\ +\psi_{i,j,k}(t)\end{array}\right\} - \sum_{i}^{N,N\neq i}\sum_{j}^{n_i,n_i\neq j}\sum_{k}^{m_j,m_j\neq k}\sigma_{(i,j,k)}\left(\zeta_{(i,j,k)},\rho_{(i,j,k)},t\right) \tag{18}$$

The last term $\sum_{i}^{N,N\neq i}\sum_{j}^{n_i,n_i\neq j}\sum_{k}^{m_j,m_j\neq k}\sigma_{(i,j,k)}\left(\zeta_{(i,j,k)},\rho_{(i,j,k)},t\right)$ indicates that the traction force has considered stress interference. The fracture length $R_{i,j,k}$ and fracture opening $w_{i,j,k}$ considering the dynamic stress of well group fracturing are further derived from the traction force:

$$R_{i,j,k}(t) = \gamma_{i,j,k}(t)\cdot\left(\left(\frac{E't}{\mu_{i,j,k}^{c}(t)}\right)^{1/3}\int_0^t Q_{i,j,k}(t)\mathrm{d}t\right)^{1/3} \tag{19}$$

$$w_{i,j,k}(r,t) = \frac{8R_{i,j,k}}{\pi E'}\cdot\int_{\rho_i}^{1}\frac{s}{\sqrt{s^2-{\rho_i}^2}}\int_0^1\frac{xT_{i,j,k}\left(\rho_{i,j,k},\mu_{i,j,k}^{c},\psi_{i,j,k}\right)}{\sqrt{1-x^2}}\mathrm{d}x\mathrm{d}s \tag{20}$$

This enables simulation of fracture propagation under different perforation-parameter combinations, thereby making it possible to optimize the number and diameter of perforation holes.

2.3. Consideration of poroelastic effects and model extensibility

The reviewer raises a pertinent point regarding the applicability of the proposed SCP framework and its underlying power balance method to scenarios involving parallel permeable cracks within a poroelastic medium. We acknowledge that fully coupled poroelastic effects can significantly influence the stress field, pore pressure distribution, and consequently, the fracture propagation and interaction dynamics (Detournay and Cheng, 1993). While the primary focus and numerical experiments presented in this manuscript are based on a linear elastic, permeable rock assumption to clearly isolate and demonstrate the core SCP concept, our methodological framework is designed with extensibility in mind.

The core of our model is a global power balance that determines fluid distribution and fracture geometry. To integrate poroelasticity, the formulation begins by modifying the expression for the normal traction, **T**, acting on the fracture faces to account for the pore pressure, p:

$$\mathbf{T} = p_{\mathrm{f}} - \sigma_{\mathrm{o}} - \sigma I - \alpha p I \tag{21}$$

where α is the Biot coefficient and I is the identity tensor. This modifies the net pressure driving fracture opening. The coupled system involving fracture width w (r,t) and traction $\mathbf{T}$ is then governed by a nonlocal integral relation from elasticity (e.g., Sneddon, 1951):

$$w_{i,j,k}(r,t) = \frac{8R_{i,j,k}}{\pi E'} \cdot \int_{\rho_i}^{1} \frac{s}{\sqrt{s^2 - {\rho_i}^2}} \int_{0}^{1} \frac{x\mathbf{T}}{\sqrt{1-x^2}} \mathrm{d}x\mathrm{d}s \tag{22}$$

The solution process iteratively enforces volume balance, $w(r, t)$, to solve for the fracture radius and opening. These are then substituted into the calculation of the various power components in the updated balance equation:

$$p_{\mathrm{f}(i)}(R_w,t)Q_i(t) = D_{\mathrm{C}(i)} + D_{\mathrm{f}(i)} + D_{\mathrm{L}(i)} + \dot{U}_i - \dot{W}_{I(i)} - \dot{W}_{\mathrm{o}(i)} + P_{\mathrm{perf}(i)} \tag{23}$$

Here, the terms for strain energy rate $\dot{U}_i$, interaction work rate $\dot{W}_{I(i)}$, and in-situ stress work rate $\dot{W}_{\mathrm{o}(i)}$ would inherently incorporate the modified traction $\mathbf{T}$ that now includes the poroelastic backstress $-\alpha p\mathbf{I}$. Furthermore, the fluid loss dissipation term $D_{\mathrm{L}(i)}$ provides a direct pathway to link leakoff with near-tip pore pressure evolution.

This outlines a pathway to build a partially coupled poroelastic model where the pore pressure field p could be prescribed from an external solution or approximated analytically. The final system would be closed by coupling the fracture propagation equations with a reservoir flow equation for p, subject to appropriate boundary conditions at the fracture faces.

However, we emphasize that a rigorous, fully coupled 3D poroelastic-hydraulic-mechanical implementation is highly complex and computationally intensive, involving the resolution of coupled pressure diffusion and stress alteration around multiple, dynamically growing fractures. Such an undertaking extends beyond the primary scope of this paper, which is to introduce and validate the SCP concept within a fundamental mechanical framework. The derivations above confirm the principled extensibility of our power-balance-based approach to incorporate poroelasticity. Future work will focus on implementing this extended formulation, validating it against analytical benchmarks for poroelastic fracture propagation, and investigating the quantitative impact of poroelastic effects on the SCP technique's efficiency in permeable formations.

2.4. Parameter optimization

The formula proposed by Fisher et al. (2002) reveals the most direct connection between well productivity q and fracture area A (Crump and Conway, 1988):

$$q \approx kh\Delta pA/\mu\Delta xh \tag{24}$$

The fracture area obtained by model simulation directly reflects the level of productivity because it is positively correlated with the stimulated reservoir volume (SRV) (Fisher et al., 2002; Cipolla et al., 2011; Hui et al., 2023c). Considering the extension of simulated fractures driven by fluid, the energy of fractures is mainly dissipated in the form of fluid flow rather than fracture rupture, such that fractures will tend to expand in a circular shape (Dontsov and Suarez-Rivera, 2020; Cheng, 2021), so the fracture area uses circular surface area: $A = \sum_{i=1}^{n} {R_i}^2\pi$. Here n is the number of perforation clusters in a single stage. With the increasing use of EXL in more and more oilfields, the accompanying high energy consumption problem leads to carbon emissions and other negative environmental footprints. Considering this factor, the design goal of SCP is: while maintaining the fracture area equivalent to EXL, the fracturing energy consumption should be minimized. Therefore, the energy consumption per unit fracture area is used as the optimization target function, and a universal method of perforation parameter optimization is established to meet the needs of single well and well group under any geological conditions. Its formula is as follows:

$$E_{\mathrm{f}} = \frac{\sum\limits_{k=1}^{N} \int_{0}^{T} p_{\mathrm{fo}(k)}(t) Q_{\mathrm{o}(k)} \mathrm{d}t}{\sum\limits_{k=1}^{N} \sum\limits_{i=1}^{n} {R_i}^2 \pi} \tag{25}$$

where k is the k-th stage of a single well, N is the total number of stages, E_{f} is the energy consumption per unit fracture area, kwh/m^2. To solve the multi-objective optimization problem (MOOP), the energy consumption per unit fractured area, the total fracture area, and the coefficient of variation of fracture area are taken as the objective functions. The corresponding function ΔE, function ΔA, and function ΔD are introduced as follows:

$$\Delta E = \left[\frac{\left(E_{\mathrm{f}(m)} - \mathrm{Max}\left(E_{\mathrm{f}(m)}\right)\right)}{\mathrm{Max}\left(E_{\mathrm{f}(m)}\right)}\right]^2 \tag{26}$$

$$\Delta A = \left[\frac{(A_{\mathrm{T}(m)} - \mathrm{Max}(A_{\mathrm{T}(m)}))}{\mathrm{Max}(A_{\mathrm{T}(m)})}\right]^2 \tag{27}$$

$$\Delta D = \left[\frac{(D_{\mathrm{A}(m)} - \mathrm{Max}(D_{\mathrm{A}(m)}))}{\mathrm{Max}(D_{\mathrm{A}(m)})}\right]^2 \tag{28}$$

In the formula, m represents the total number of test perforation parameter samples, and $E_{\mathrm{f}(m)}$ is the energy consumption per unit fractured area of the m-th test. $A_{\mathrm{T}(m)}$ is the total fractured area of the m-th test. $D_{\mathrm{A}(m)}$ is the standard deviation of fracture area of the m-th test.

2.5. Algorithm

Most of the commonly used fracturing simulation software are limited by computation efficiency, so fracturing parameter optimization design adopts a decoupling method, which is, only one parameter is allowed to vary, while other parameters to be optimized are set to fixed values. Once a parameter is optimized, it is fixed, and then other parameters are optimized one by one. However, in the actual process of fracture expansion, multiple parameters interact with each other, and decoupling optimization cannot achieve the expected optimization effect.

Unlike conventional methods, the semi-numerical C5Frac simulation model (Cheng and Bunger, 2016), combines approximate solutions with energy law, enhancing computation speed while ensuring precision. This enables the coupled optimization of perforation parameters based on dynamic stress distribution, effectively reducing the energy consumption in hydraulic fracturing. The algorithm for parameter optimization in SCP proceeds as follows (Fig. 2):

S1—Setting initial parameters such as reservoir rock mechanics, stage and cluster, pumping procedure and so on, including $\sigma_{\min}, C_{\mathrm{L}}, E, \vartheta, \mu, K_{\mathrm{I}}, Q_{\mathrm{o}}, T, \Delta t, h_i, Z$ etc., where $\sigma_{\min}$ is the minimum in-situ stress; C_{L} is the leakoff factor, used to describe the sealing

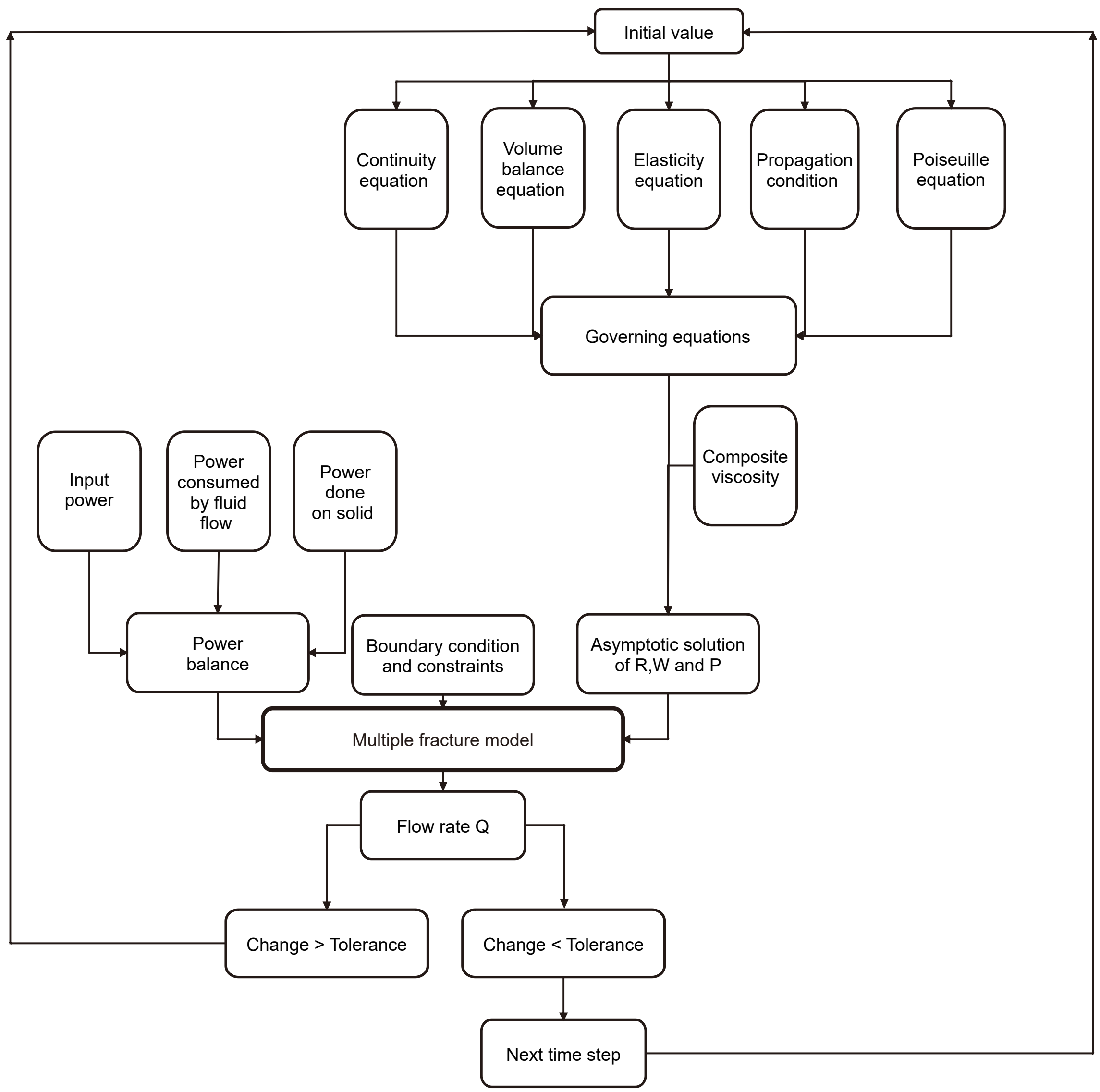

Fig. 2. Flow chart for parameter optimization in SCP.

ability of the surrounding rock to the injected fluid, affected by rock properties and fluid properties; E is Young's modulus, ϑ is Poisson's ratio, μ is fluid viscosity, K_I is rock fracture toughness, Q_o is total injection flow rate, t_p is total pumping time, Δt is time step, h_i is the distance between each perforation cluster in certain stage, and Z is stage length.

S2—Using the Monte-Carlo random method, a value is randomly selected from between 5 and 20 each time as the number of perforation holes in each perforation cluster within the stage; the diameter of the hole is randomly selected from a value between 0.006 and 0.015 m; then these two randomly selected perforation parameters are combined into a trial perforation parameter pair.

S3—The initial solution specifies $Q_i(t_\mathrm{o}) = Q_\mathrm{o}/N$, where t_o is a specified initial time (before leakage and interaction become important). If it is not the initial time, $Q_i(t)$ equals the flow rate $Q_i(t-\Delta t)$ of the previous time step.

S4—Substituting the initial iterative flow rate $Q_i(t)$ into Eqs. (18)–(20) to obtain the fracture propagation result.

S5—Updating the real-time stress distribution using Eq. (12). Then calculating the power required for a fracture to overcome stresses induced by previously fractured fractures using Eq. (14). Next, calculating the fluid power loss across the perforations using Eq. (17), and substituting all power terms into the power-balance equation.

S6—As shown in the flowchart, the value of $Q_i(t)$ is iteratively updated until that the change of $Q_i(t)$ is smaller than the tolerance.

S7—After obtaining $Q_i(t)$, repeat steps S3–S6 until the total pumping time t_p is obtained. Then use Eq. (22) to accumulate the total fracture area within a single stage.

S8—Repeating S3–S7, the fracture growth of all stages in a single well and the corresponding total energy consumption is achieved. Then the energy consumption of unit fracturing area of the perforation parameters pair is obtained through Eq. (23).

S9—Repeating S2–S8 until all possible combinations ($16 \times 10 = 160$) of perforation number and perforation diameter are simulated. Finally, on the premise that the volume of the injected fluid is equal, comparing the unit fracture area energy consumption E_f of each combination of perforation parameters, and selecting the perforation-parameter combination that achieves the maximum fracture area with the minimum energy consumption.

The implementation of the above algorithmic process relies on the self-developed semi-numerical simulator C5Frac. This simulator offers sufficient precision while maintaining computational efficiency, enabling tens of thousands of evaluations to be run within a manageable time. The graphical parameter input interface of the program is developed based on MATLAB GUI, and the runtime environment of the program-including the command window and workspace is shown in Fig. 3.

3. Model validation

3.1. Single fracture

The benchmark solution is calculated by Dontsov (2016) by developing a numerical approximation for a penny-shaped hydraulic fracture. This solution captures the transition behavior of hydraulic fractures between negligible and large leakoff and between large viscosity and large toughness regimes. It is also accurate in capturing limiting behavior for toughness or viscosity dominated and leakoff or storage dominated hydraulic fractures. To better visualize the approximation, the validation is separated as two parts. First part is time variation for given parameters $E' = 9.5$ GPa, $K_{\mathrm{IC}} = 10^7$ Pa·m$^{1/2}$, $\mu = 0.001$ Pa·s, $Q_{\mathrm{o}} = 0.01$ m^3/s. Additionally, the choice of the leakoff parameter is $C_{\mathrm{L}} = \{10^{-5}, 10^{-4}, 10^{-3}$ m/s$^{1/2}\}$. As can be seen from Fig. 4, all quantities match the reference solution within one percent. The only exception is oscillatory behavior in the efficiency for large values of C_{L}; but here the oscillatory behavior is in the reference solution, not our approximate solution. This comparison uses relatively large toughness and can be shown to correspond to the toughness dominated and near-toughness dominated transition regimes.

To further check the accuracy of the approximate solution, smaller toughness is also used and parameters are set as $E' = 9.5$ GPa, $K_{\mathrm{IC}} = 1000$ Pa·m$^{1/2}$, $\mu = 1$ Pa s, $Q_{\mathrm{o}} = 0.1$ m^3/s. Additionally, the choice of the leakoff parameter is $C_{\mathrm{L}} = \{10^{-5}, 10^{-4}, 10^{-3}$ m/s$^{1/2}\}$. Similar to the large toughness cases shown in Fig. 4, the accuracy of all quantities is under 1%, as can be seen from Fig. 5.

To further quantify the level of accuracy of the approximation, a relative error is defined as

$$\mathrm{Err} = \sqrt{\left[\frac{x_{\mathrm{ref}} - x_{\mathrm{apr}}}{x_{\mathrm{ref}}}\right]^2} \tag{29}$$

where subscripts ref and apr correspond to the reference and approximation solution respectively. Here the variable x can be the fracture radius R, the efficiency η, or the wellbore width W.

To demonstrate the accuracy, which is affected by several parameters, it is important to note that the error is demonstrated versus the dimensionless time $\lg(\tau)$ and leakoff parameter $\lg(\Phi)$, given as Eqs. (27) and (28) (after Dontsov, 2016).

$$\phi = \frac{C_{\mathrm{L}}'^4 Q_{\mathrm{o}} E'^{11} \mu'^3}{K'^{14}} \tag{30}$$

$$\tau = \left(\frac{K'^{18} t^2}{E'^{13} \mu'^5 Q_{\mathrm{o}}^3}\right)^{1/2} \tag{31}$$

These dimensionless quantities can be used to characterize a globally-defined propagation regime for each fracture, as detailed by Dontsov (2016). The regimes validity zones are denoted in Figs. 6–8 as:

(1) M (viscosity–storage) regime, corresponding to viscous dissipation far exceeding dissipation associated with the fracture toughness, and negligible fluid leakoff rate compared to the rate of change of the fracture opening (width).

(2) K (toughness–storage) regime, corresponding to negligible dissipation associated with fluid flow as well as negligible leakoff rate.

(3) $\tilde{M}$ (viscosity–leakoff) regime, corresponding to dominant viscous dissipation and large fluid leakoff velocity compared to the rate of change of the fracture width.

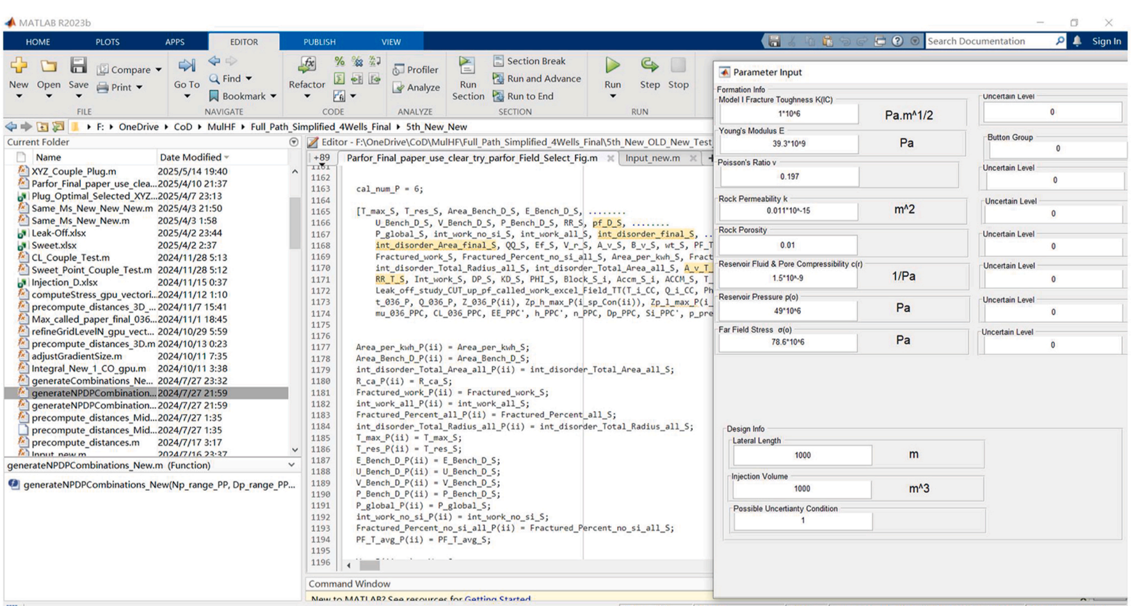

Fig. 3. A complete screenshot of the graphical user interface (GUI), the MATLAB runtime workspace, and the command window.

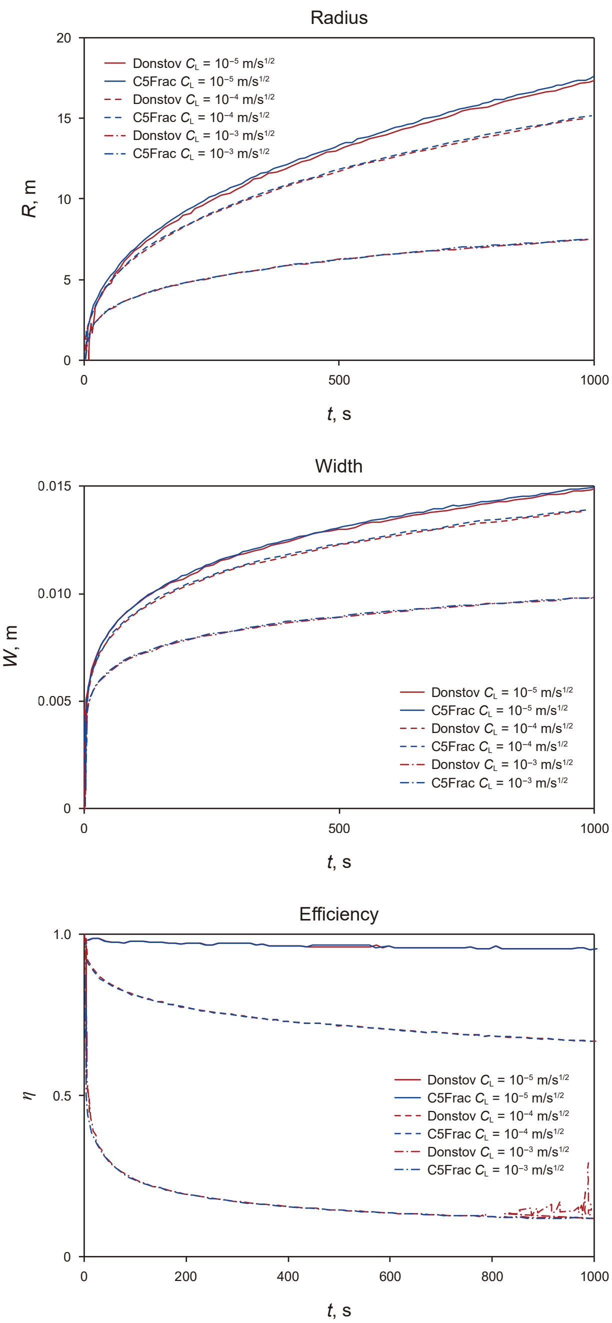

Fig. 4. Single fracture validation at large toughness. Comparison between the approximation solution (blue line) and the reference solution (red line) in terms of time histories of: fracture radius, width at the wellbore ($\rho = 0$) and efficiency. Dotted, dashed and solid lines indicate the $C_L = \{10^{-3}, 10^{-4}, 10^{-5}\ \mathrm{m/s^{1/2}}\}$ respectively. See online version of the article for full color.

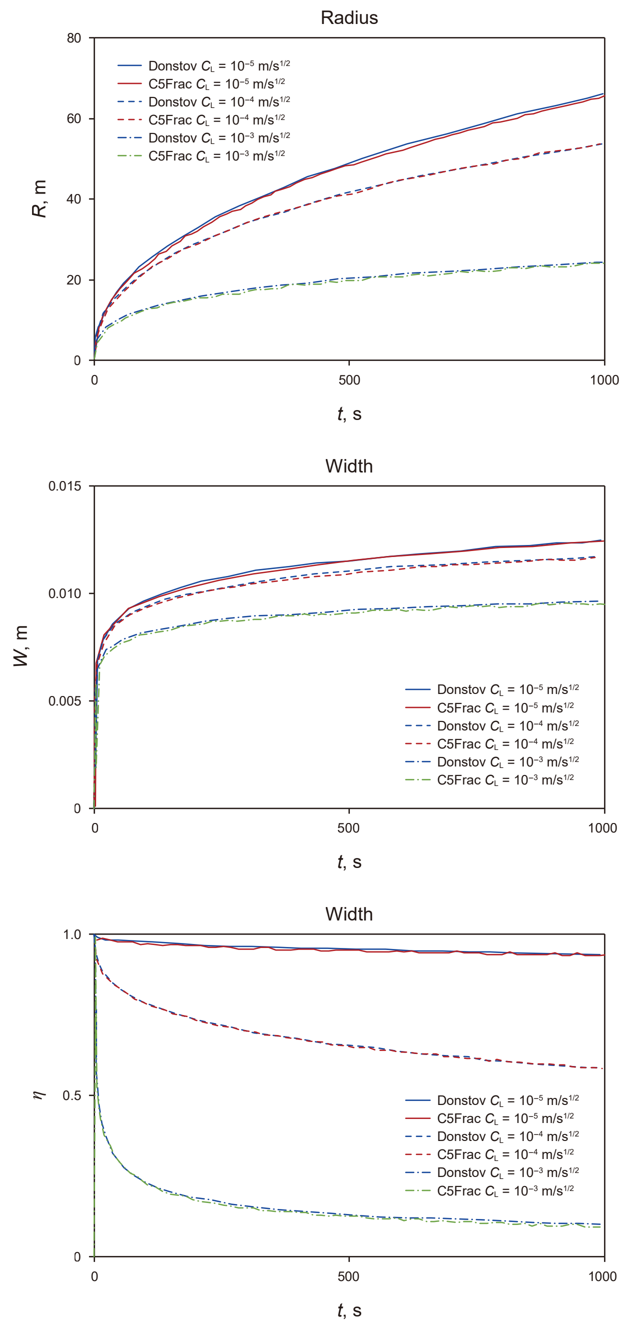

Fig. 5. Single fracture validation at small toughness. Comparison between the approximation solution (blue line) and the reference solution (red line) in terms of time histories of: fracture radius, width at the wellbore ($\rho = 0$) and efficiency. Dotted, dashed and solid lines indicate the $C_L = \{10^{-3}, 10^{-4}, 10^{-5}\ \mathrm{m/s^{1/2}}\}$ respectively. See online version of the article for full color.

(4) $\tilde{K}$ (toughness–leakoff) regime, corresponding to negligible fluid viscosity and large fluid leakoff rate.

It is important to note here that the fracture propagation regimes are defined for a single planar fracture with steady flow rate. To visualize the propagation regimes, Figs. 6–8 plot the validity zones corresponding to the limiting asymptotic solutions corresponding to each of these limiting regimes. The transitions between the regimes are where numerical solutions are needed, in general, or some other suitable approximations (as provided e.g., by Dontsov, 2016).

As Fig. 5 shows, the relative error in the radius prediction compared to the reference solution is less than 1% in most regions, but it rises to a maximum of around 7% in the small leakoff transition between the viscosity and toughness dominated regimes. Similarly, Fig. 6 shows that the relative error on fracture width (i.e., crack opening) in most regions is below 1%, but with more significant mismatch (up to 20%) in the large leakoff transition between the viscosity and toughness dominated regimes. Note that

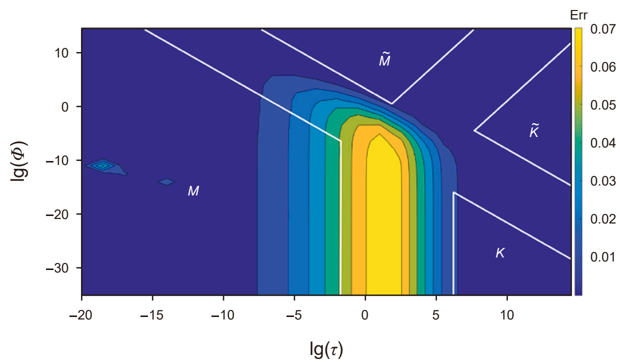

Fig. 6. Test accuracy for radius. Relative error associated with the approximate fracture length (radius) solution R versus dimensionless time τ and leakoff parameter Φ. M, K, $\tilde{M}$ and $\tilde{K}$ regions indicate, respectively, validity zones of the M vertex solution, K vertex solution, $\tilde{M}$ vertex solution and $\tilde{K}$ vertex solution, according to Dontsov (2016). White lines indicate boundaries of applicability of the vertex solutions.

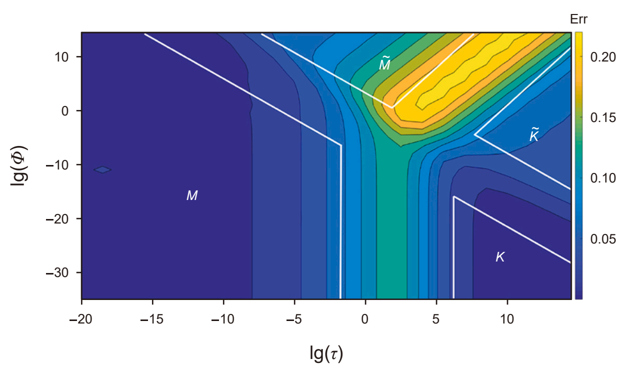

Fig. 7. Test accuracy for width. Relative error between approximate and reference solutions for crack opening at inlet W. These are shown as they vary with dimensionless time τ and leakoff parameter Φ. M, K, $\tilde{M}$ and $\tilde{K}$ regions indicate, respectively, validity zones of the M vertex solution, K vertex solution, $\tilde{M}$ vertex solution and $\tilde{K}$ vertex solution (Dontsov, 2016). White lines indicate boundaries of applicability of the vertex solutions.

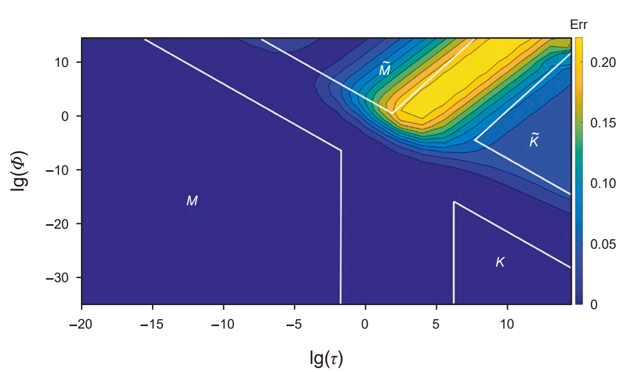

Fig. 8. Test accuracy for efficiency. Relative error between approximate and reference solutions for efficiency η. These are shown as they vary with dimensionless time τ and leakoff parameter Φ. M, K, $\tilde{M}$ and $\tilde{K}$ regions indicate, respectively, validity zones of the M vertex solution, K vertex solution, $\tilde{M}$ vertex solution and $\tilde{K}$ vertex solution (Dontsov, 2016). White lines indicate boundaries of applicability of the vertex solutions.

this particular region will often be of little relevance. For the combination of parameters used here, this range was obtained for the leak-off coefficient C_L being greater than 10^4 m/s$^{1/2}$, which can be compared to a practical range of 10^{-4} to 10^{-5} m/s$^{1/2}$. Such a large value of C_L leads to a 10^{-5} m crack opening and 10^{-11} efficiency, which means that a tiny absolute difference between the approximation and reference solution will result in a large relative difference. That is why there is a 20% difference shown in Figs. 6 and 7. Otherwise, the match is very good and the approximation is shown to suitably replicate the correct radius, width, and efficiency across all relevant ranges of parameter values.

3.2. Multiple fractures

Having demonstrated accuracy for single fracture growth relative to a single fracture reference solution, the level of accuracy of the developed approximation for multiple fractures will be quantified relative to reference solutions from a high-fidelity hydraulic fracture simulator (Chen et al., 2019; Huang et al., 2024; Sesetty and Ghassemi, 2013). The high-fidelity model used here is a fully coupled simulator called ILSA II (Peirce and Bunger, 2015), which is extended for multiple, parallel planar hydraulic fractures based on the implicit level set algorithm, (ILSA) (Peirce and Detournay, 2008). The key novelty of ILSA that makes it suitable as a benchmark simulator for our purposes is its enabling accurate solutions on very coarse meshes by embedding appropriate tip asymptotic behavior and then tracking moving boundary using a level set method that projects the front location based on these known asymptotics. This allows it to overcome common challenges in hydraulic fracture simulation of mesh sensitivity and time step limiting stability criteria, both of which can lead to either inaccurate solutions or large computational times. In ILSA, the elasticity equation is solved using a 3D displacement discontinuity method (Crouch and Starfield, 1983) and fluid flow is solved locally using the finite volume method. We benchmark and illustrate the use of the model considering cases with 5 HFs. The fractures are placed symmetrically relative to the middle fracture. Hence the "outer" fractures, 1 and 5, are identical. Also, the "inner" fractures, 2 and 4, are identical. Fracture 3 always occupies the center of the array and will henceforth be called the "middle" fracture. The following parameter set is used for both the C5Frac and ILSA II simulations:

$$C_L = 0 \text{ m/s}^{1/2}, E = 9.5 \text{ GPa}, \nu = 0.2$$

$$\sigma_o = 70 \text{ MPa}, R_W = 0.2 \text{ m}$$

To better understand the effect of toughness, two benchmarking cases considering uniform and non-uniform spacing between the fractures are chosen. One case is $\mu = 1$ Pa·s, $K_{IC} = 0$ MPa·m$^{1/2}$, $Q_o = 0.1$ m^3/s, $Z = 20$ m. Another case is $\mu = 0.001$ Pa·s, $K_{IC} = 1.5$ MPa m$^{1/2}$ $Q_o = 0.0265$ m^3/s, $Z = 120$ m. For each case, we present comparisons of the time evolution of fracture radius, fluid influx to each fracture, fracture opening at the center, and total fracture area. Specifically, Fig. 9 is the case where the fractures are uniformly spaced so that $h_1 = 30$ m, the stage length z is 120 m, so the fracture planes have z coordinates $z_1 = 0$, $z_2 = 30$, $z_3 = 60$, $z_4 = 90$, and $z_5 = 120$. In Fig. 10, we introduce a modification to the uniform array in which fractures 2 and 4 are moved, and also stage length is changed to be $z = 20$ m, so that $h_1 = 3.6$, corresponding to fracture planes having z coordinates $z_1 = 0$, $z_2 = 3.6$, $z_3 = 10$, $z_4 = 16.4$, and $z_5 = 20$. The results presented include: a) The dimensionless radius $R_i(t)/Z$, b) the inflow rate $q_i(R_w, t)$, c) the crack aperture at inlet $w_i(R_w, t)$, and d) total fracture area defined as

$$A(t) = \sum_{i=1}^{N-1} R_i^2(t)\pi \tag{32}$$

Overall, C5Frac approximates ILSA II well. For our purposes, it is especially significant that the fracture area computed by C5Frac

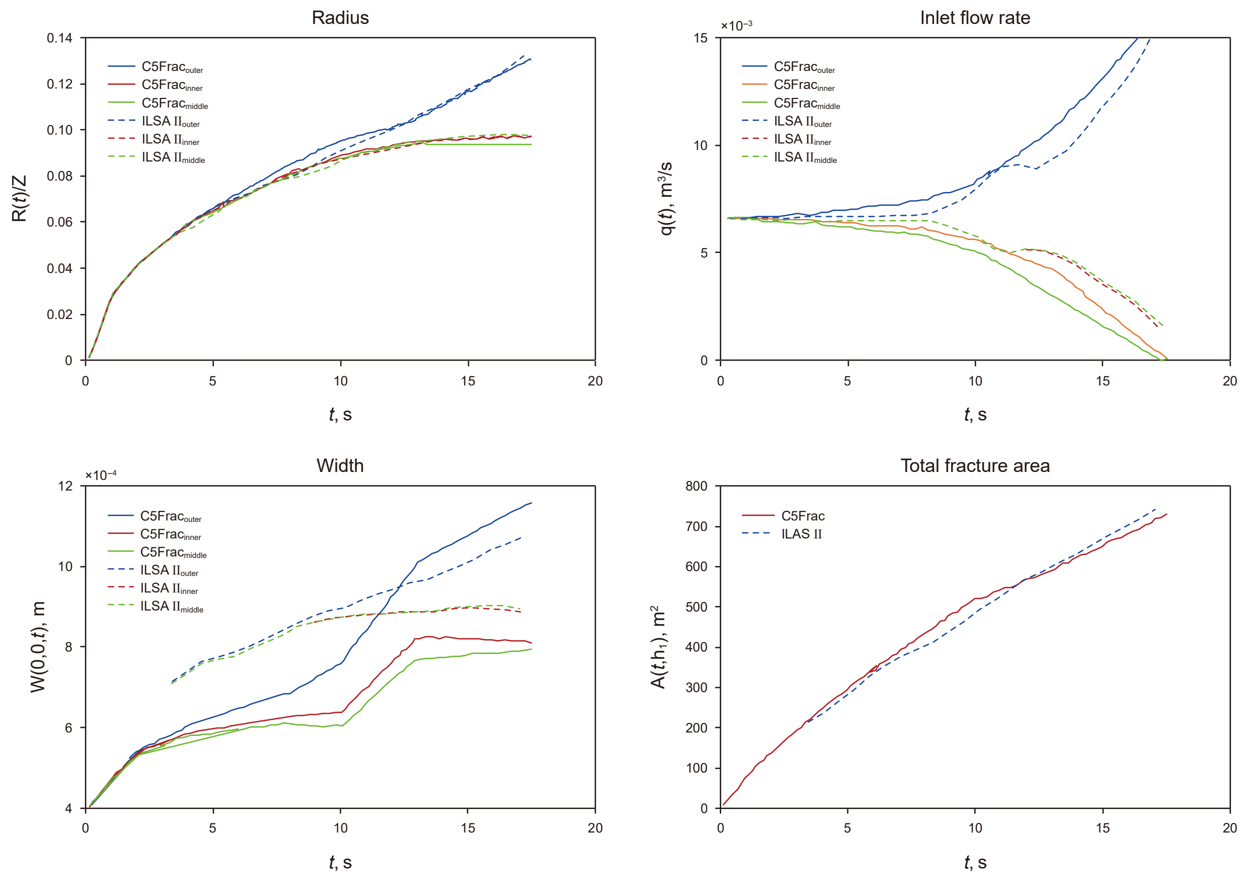

Fig. 9. Multiple fractures validation at large toughness. C5Frac compared with ILSA II for a uniform array with $h_1 = h_2 = h_3 = h_4 = 30$ m.

typically differs from that of ILSA II by less than 5%. This quantity is naturally the most important when optimization is to be carried out on the created fracture area. The inlet flux and radius also approximated reasonably, with several observation that can be made. Firstly, we observe the stress-shadowing phenomenon, in which outer fractures grow preferentially while growth of the inner fractures is stunted instead of uniform growth. This is strongly evidenced in the uniform spacing case (Fig. 9), where the inflow to the outer fracture increases sharply to 0.013 m^3/s and consumes nearly all the total injection rate after 15 s. The localization of growth in the outer fractures is understandable because they have no constraint like the previous stage effect on their growth from outside the array. At the same time, flow rate to the other fractures decreases to approach zero. This is understood because the interior fractures have to compete with one another in an induced compressive stress field that is established by the outer fractures and enhanced by any additional growth by the interior fractures. The localization to the outer fractures becomes more pronounced with time while growth of the inner fractures is minimal for uniform $h_1 = 30$ m case (see Fig. 9).

In comparison to the uniform spacing cases, approximation is more difficult to obtain for the non-uniform spacing cases. The main reason is a complicated behavior associated with coupling among the fractures that has previously been called “squeeze out effect” (Cheng and Bunger, 2019a, 2019b; Peirce and Bunger, 2015). When this phenomenon occurs, the non-uniform growth plays a crucial role to promote a decreasing interaction work of initially suppressed fractures. Thus, fluid flow within the inner fractures becomes dominant, in this example, after 100 s (Fig. 10). At the same time, the swelling inner fractures induce a compressive force which has the effect of advancing the fracture by the displacing the fluid from the vicinity of the wellbore rather than by influx from the wellbore. The outer and middle fractures get a chance to grow after this reversal. In addition, more fractured area is achieved compared with the uniform spacing cases. This occurs, because the fracture growth becomes more uniform.

The accuracy has been demonstrated by suitable agreement between C5Frac and ILSA II in both uniform and non-uniform spacing cases. Furthermore, identifying the opportunities to reduce environmental footprint, which requires hundreds to thousands of model evaluations, is enabled by the calculation speed. To this point, an illustration of computation time for C2Frac (Cheng and Bunger, 2016), C3Frac (Cheng and Bunger, 2019a), and ILSA II (Peirce and Bunger, 2015) is presented in Table 1.

C5Frac takes only minutes to compute a single multi-fracture result at typical reservoir length and time scales on a personal computer. Although this is much slower than C2Frac, which computes in a few seconds, and also twice slower than C3Frac, the benefit is the ability to simulate the leakoff and toughness (available only in C5Frac) effects. And most strikingly, the simulations are much faster than fully coupled simulations, which can take tens of hours and up to a week to compute on a similar computer. Note that the computation time of ILSA II for each time step continuously increases because the advancing front leads to an ever-increasing number of elements in the simulation, there is no such increase in computation time per model time step in C5Frac. So, in conclusion, because of the reasonable accuracy at high calculation speed, this new approximate simulator opens new possibilities to explore large parametric spaces, identifying combinations of parameters associated with high resource use efficiency (i.e., minimizing volume cost per recovery).

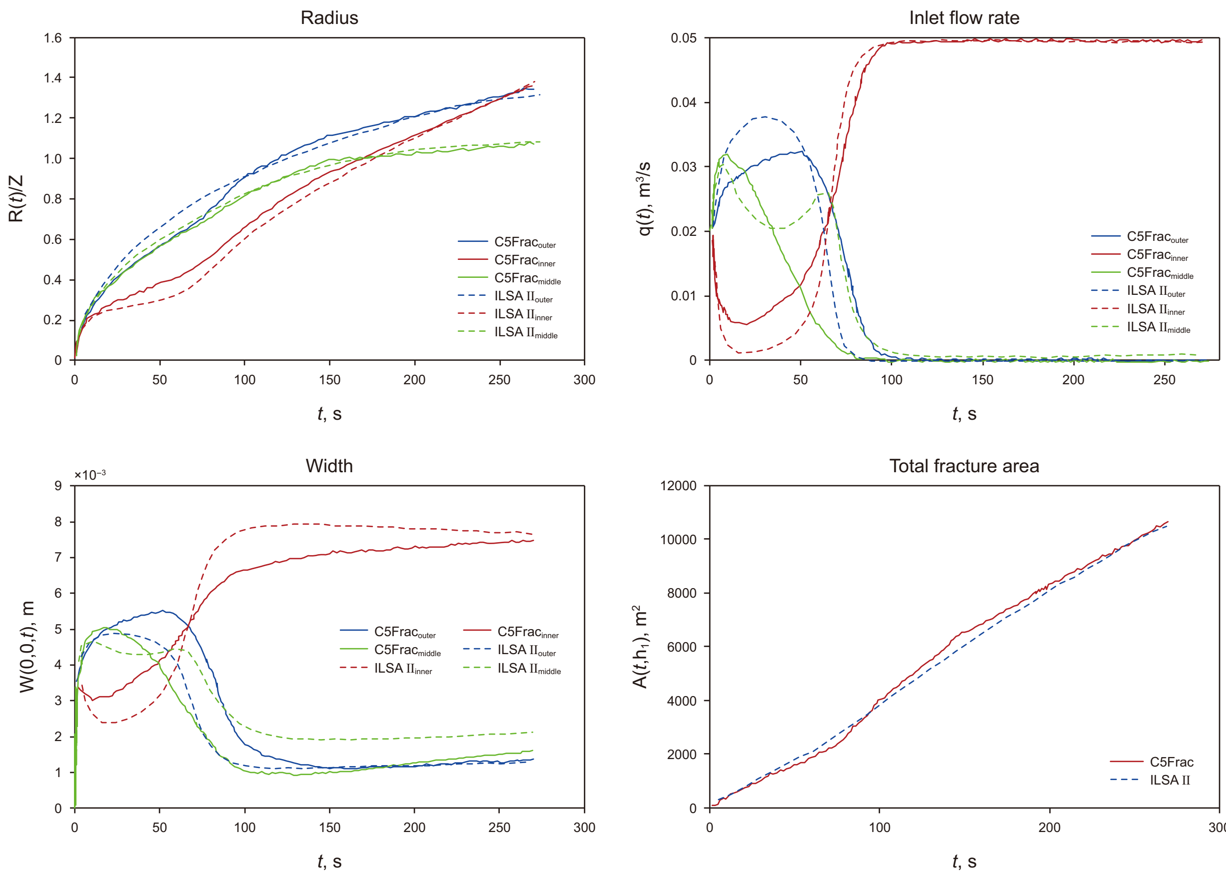

Fig. 10. Multiple fractures validation at small toughness. C5Frac compared with ILSA II for non-uniform array with $h_1 = h_4 = 3.6$ m and $h_2 = h_3 = 6.4$ m.

Table 1
Timing comparison of different uniform.

Uniform five	C2Frac	C3frac	C5frac	ILSA II
Computation time, s	1.06	255	686	220612
Simulation time, s	203	203	203	203
Number of steps	128	128	128	128
Processer & RAM	INTEL-i7 4770 k 4.00 GHz 32 GB RAM	INTEL-i7 4770 k 4.00 GHz 32 GB RAM	INTEL-i7 4770 k 4.00 GHz 32 GB RAM	INTEL-XEON E5649 2.53 GHz 96 GB RAM

3.3. Trial data compare

As the figure shown, the simulation result could capture the changing tendency of seismic data in general (Fig. 11). Especially in the red region, the fracture length given by simulation could approximate seismic data in several percent.

4. Results and discussion

The effectiveness of EXL and SCP is compared through two cases. Case one is a single well in homogeneous reservoir to illustrate the basic mechanism of SCP. Each stage is designed with a spacing of 60 m and contains five symmetrically arranged perforation clusters, spaced 12.5 m apart. The first cluster at the toe end is positioned 5 m from the bridge plug, and the first cluster at the heel end is likewise 5 m from the corresponding bridge plug.

Case two is a real field trial conducted in the Fan Ye 1 well factory. It involves four horizontal wells. These wells have trajectories that extend in roughly the same direction but are not parallel to each other. The spacing between the horizontal wells ranges from 200 to 800 m. Their vertical depths differ by approximately 100 m. The target zone is essentially located in the same reservoir, and the heterogeneity of reservoir parameters such as porosity and permeability around the wellbore is strong, and hence the variability of the leakoff coefficient along the wellbore is large.

Based on the aforementioned perforation parameter optimization method, two strategies were developed. Strategy one: for the reservoir with weak homogeneity, to reduce operational complexity, globally optimizing a set of SCP parameters for all stages called global stress coupled perforation (G-SCP) is preferable. Strategy two: for more heterogeneous reservoir, optimizing perforation parameters stage by stage. The optimization of perforation parameters for each stage is based on the stress field of the operating stage, named stage stress coupled perforation (S-SCP). This approach is taken to minimize the heterogeneity between stages as much as possible. According to the number of stages in field and the intensity of reservoir heterogeneity, the computational resources consumed the global G-SCP and local S-SCP stress coupled perforation are used flexibly. Meanwhile, enhancing computational efficiency and reducing computational requirements also provide an alternative approach to optimizing energy consumption.

As the comparison in both cases, the parameters for EXL are 5 holes per cluster and a hole diameter of 6 mm; the selection range for SCP parameters is 5 to 20 holes per cluster and hole diameters ranging from 6 to 15 mm (Fig. 12).

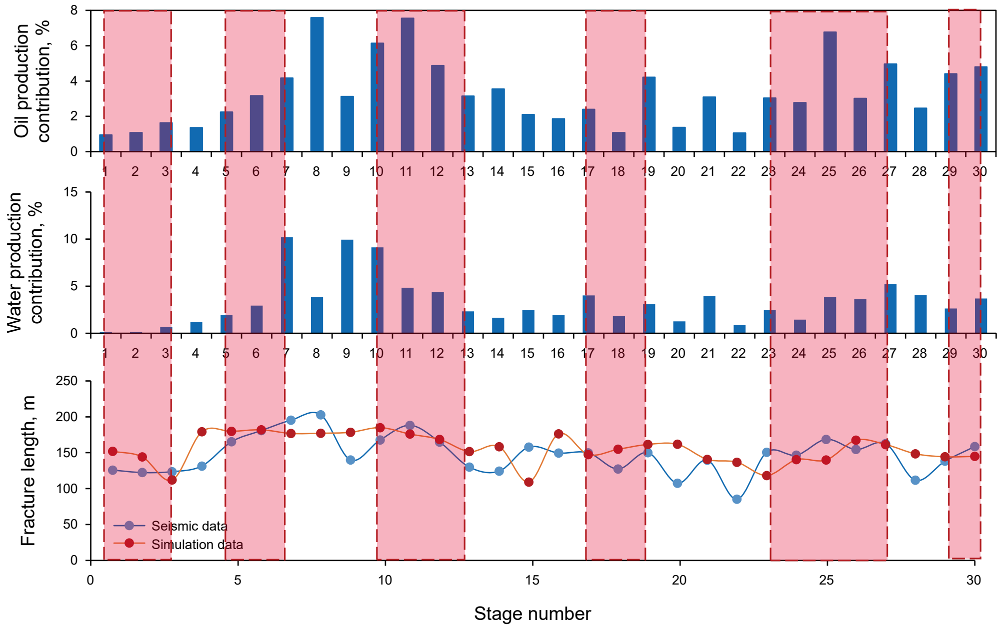

Fig. 11. Comparison between trial data and simulation data stage by stage along the well.

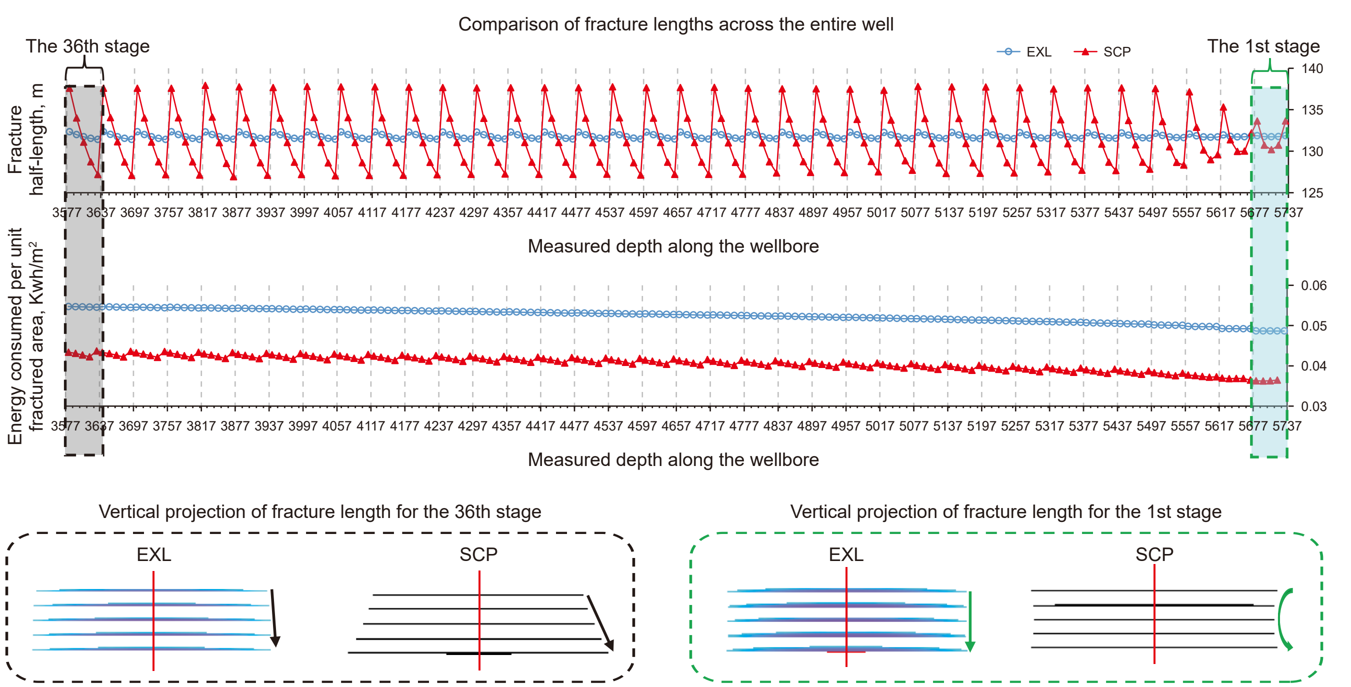

Fig. 12. Comparison of fracture half-length, energy consumption per unit fracture area, and fracture expansion between EXL and SCP. The arrows in the enlarged view of the fracture length represent the trend of the fracture length within the chosen segment towards the toe direction along the wellbore.

4.1. Example of global stress coupled perforation in homogeneous reservoir for a single well

The representative reservoir parameters and engineering parameters such as Carter leakoff coefficient, reservoir pressure, and fluid injection rate are imported into the semi-numerical model C5Frac to compare the differences between the G-SCP and the EXL (Figs. 13 and 14). The parameters are as follows:

$$C_L = 8.89 \times 10^{-6}\ \mathrm{m/s^{\frac{1}{2}}};\ E = 32.16\ \mathrm{GPa};\nu = 0.23;$$

$$C_{ro} = 1.5 \times 10^{9}\ \mathrm{Pa^{-1}};\quad K_{IC} = 1\ \mathrm{MPa{\cdot}m^{\frac{1}{2}}};$$

$$\sigma_{min} = 63.63\ \ \mathrm{MPa};\ R_W = 0.2\ \mathrm{m};\mu = 0.003\ \mathrm{Pa{\cdot}s};$$

$$P_r = 50.90\ \mathrm{MPa};\ Q_o = 0.15\ \mathrm{m^3}\Big/\mathrm{s};\ V_{inj} = 540\ \mathrm{m^3}$$

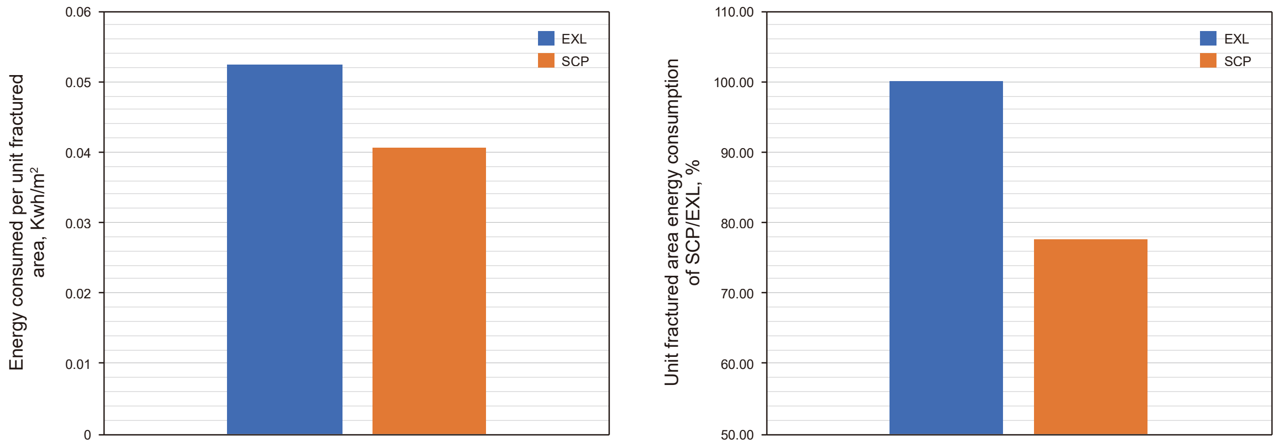

Fig. 13. Comparison of energy consumption per unit fractured area between G-SCP and the EXL.

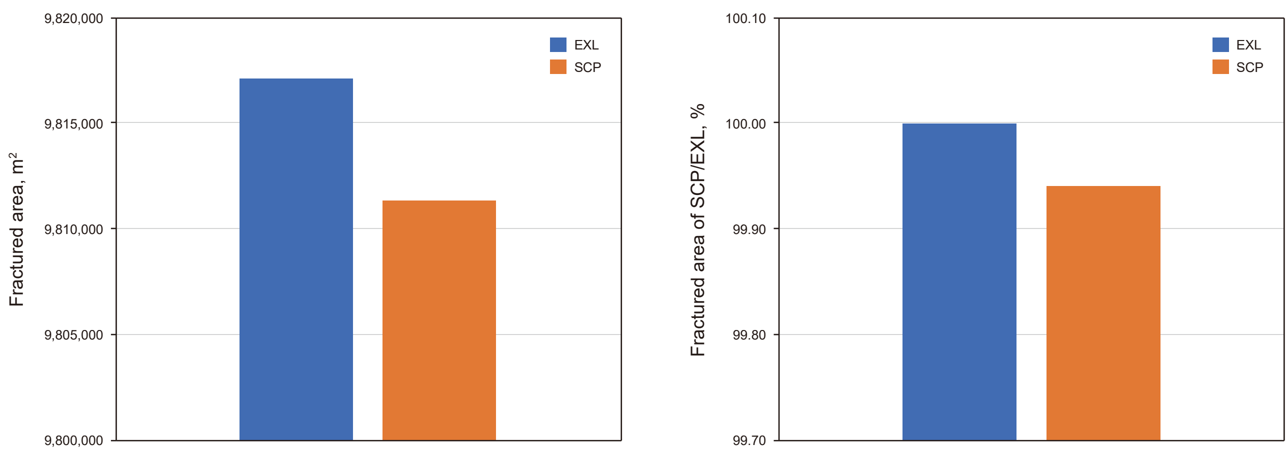

Fig. 14. Comparison of fractured area between G-SCP and the EXL.

where C_{ro} is the rock compressibility coefficient, R_W is the wellbore diameter, P_r is the reservoir pressure, and V_{inj} is the total injection volume of fluid per stage. The stage length is set as 60 m that commonly used, with 5 perforation clusters distributed symmetrically about the center, with a spacing of 12.5 m. The distance between the perforation clusters at both ends and the plug is 5 m. The lateral length is 2160 m, with a total of 36 stages. The Monte Carlo method is used to randomly combine perforation number and perforation diameter to generate candidate parameter sets for the numerical experiments. After the fully coupled computation, the design parameters of the G-SCP are finally obtained, as shown in Table 2.

The simulation results show that no matter what kind of perforation technique is used, the fractures at both ends in the first three stages close to the toe are subject to less stress, allowing more fluid to enter and forming dominant fractures; the fractures in the middle are relatively suppressed. As stress accumulates, this phenomenon gradually changes in operation sequence: the length of the fracture is directly proportional to the distance from the previous operation segment. The G-SCP technique, at the cost of losing 0.1% of fracture area, has a 22% lower energy consumption per unit fracture area than the EXL technique (see Figs. 13 and 14). Therefore, for a single well in a homogeneous reservoir, the energy-saving effect of the G-SCP is indicated as significant.

Table 2
Comparison of perforation parameters of EXL and SCP for a homogeneous reservoir in a single well example.

Perforation technique type	Perforation number/cluster	Perforation hole diameter, m
EXL	10	0.01
G-SCP	17	0.012

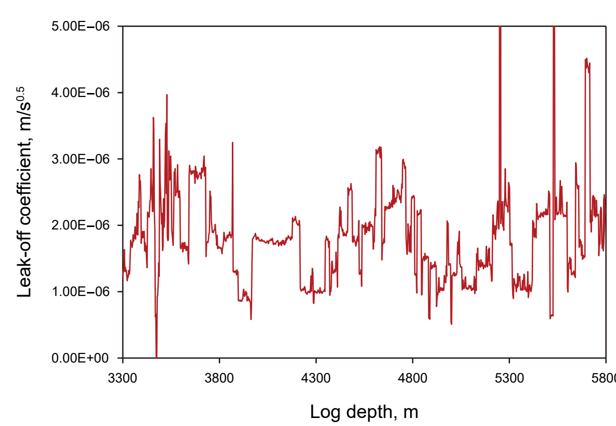

Fig. 15. Variation of formation leakoff coefficient near the wellbore with measured depth.

Tabel 3
Perforation parameters of S-SCP in first 3 stages of FY1-6 well.

Stage No.	Upper bound of the perforation clusters, m	Lower bound of the perforation clusters, m	Perforation length, m	Number of holes per stage	Diameter of perforation holes, m
1	5552.6	5553.4	0.8	40	0.006
	5540.1	5540.9	0.8		
	5527.6	5528.4	0.8		
	5515.1	5515.9	0.8		
	5502.6	5503.4	0.8		
Plug	5498				
2	5492.7	5493.3	0.6	30	0.01
	5480.2	5480.8	0.6		
	5467.7	5468.3	0.6		
	5455.2	5455.8	0.6		
	5442.7	5443.3	0.6		
Plug	5438				
3	5432.65	5433.35	0.7	35	0.008
	5420.15	5420.85	0.7		
	5407.65	5408.35	0.7		
	5395.15	5395.85	0.7		
	5382.65	5383.35	0.7		
Plug	5378				

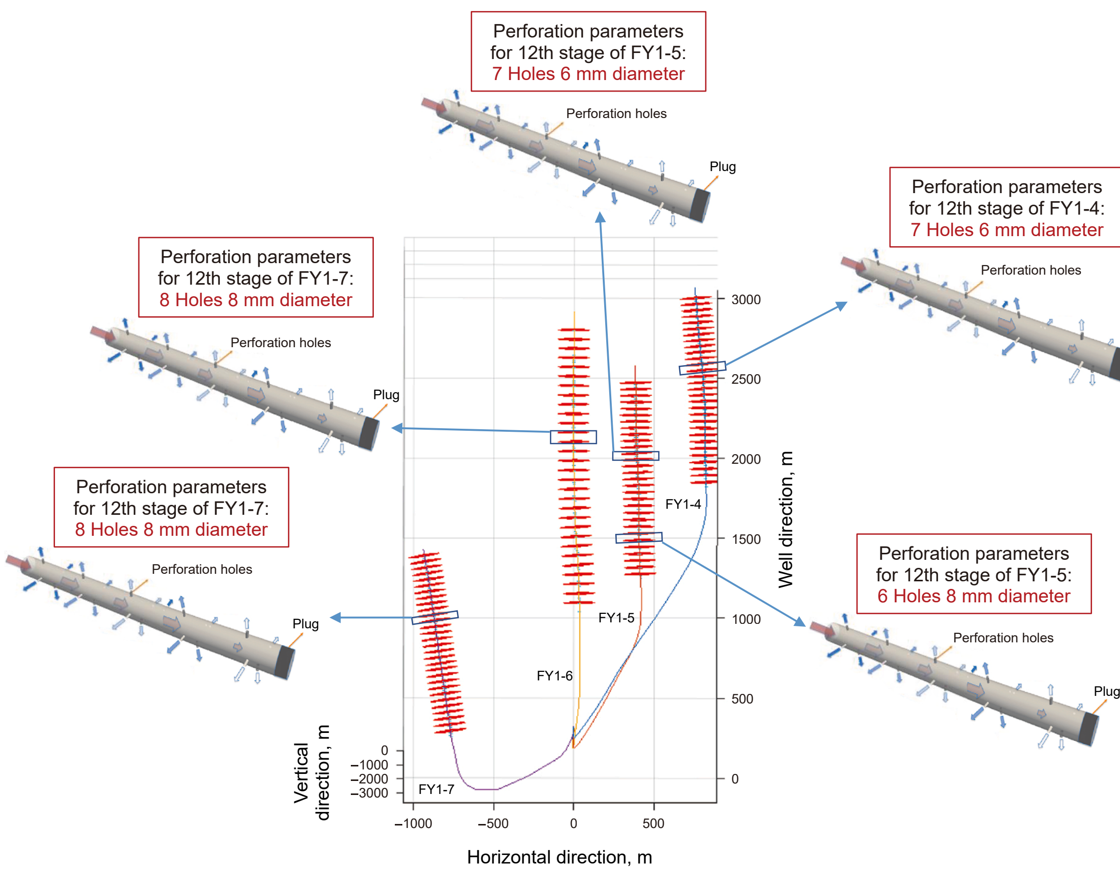

Fig. 16. Illustration of the S-SCP design parameters for Fan Ye 1 well factory.

4.2. Example of stage stress coupled perforation in heterogeneous reservoir for a well factory

After demonstrating the phenomenon by which SCP outperforms EXL in a homogeneous case, SCP is further applied to a heterogeneous reservoir. To characterize this heterogeneity, the Carter's leakoff coefficient C_L is introduced as a representative parameter.

$$C_L = (\sigma_o - p_o)\sqrt{\frac{k c_r \phi}{\pi \mu}} \tag{33}$$

Here, k denotes the rock permeability, c_r is the composite compressibility coefficient accounting for both reservoir fluid and pore compressibility, ϕ represents the rock porosity, and p_o stands for the reservoir pressure. Taking Fan-Ye 1-5 in the Fan-Ye 1 well

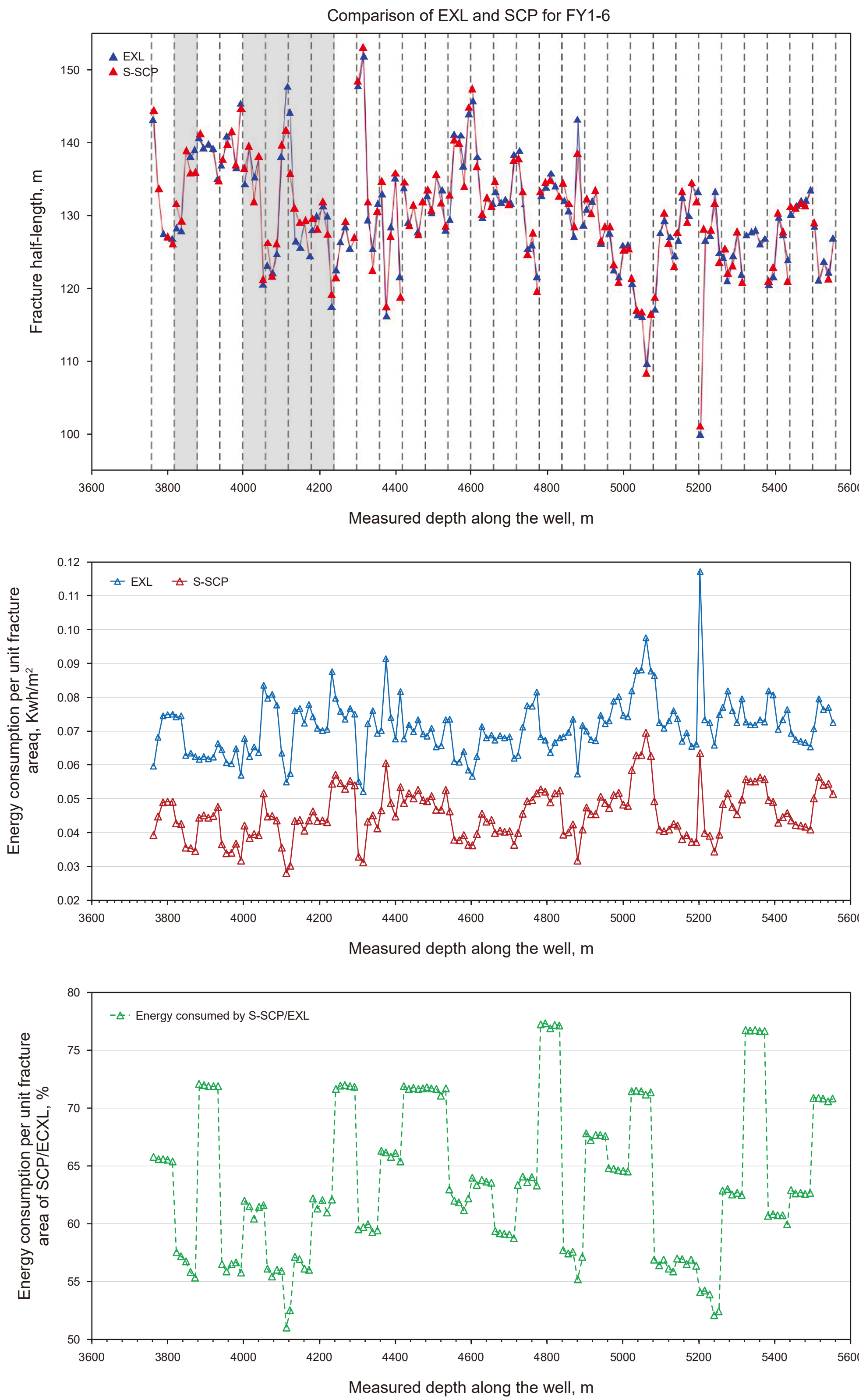

Fig. 17. In top subplot figure, the fracture length of EXL and SCP is compared. The figure in middle denotes energy consumption per unit fractured length by EXL and SCP. In above two subplots, blue line represents EXL, and the red line is S-SCP. The figure in the bottom is the ratio of energy consumed by SCP divided by EXL.

Table 4
Comparison of total fracture area and corresponding energy consumption per unit fractured area between EXL and SCP.

Comparison	Total fractured area, m^2			Energy consumption per unit fractured area, kwh/m^2		
Well No.	EXL	S-SCP	Ratio, %	EXL	S-SCP	Ratio, %
FY1-4	9077973	9078343	1.0004	0.0629	0.0451	71.586
FY1-5	9685718	9682731	99.969	0.0601	0.0407	67.665
FY1-6	7989279	7980892	99.895	0.0713	0.0455	63.783
FY1-7	9005368	9001945	99.962	0.0678	0.0426	62.793

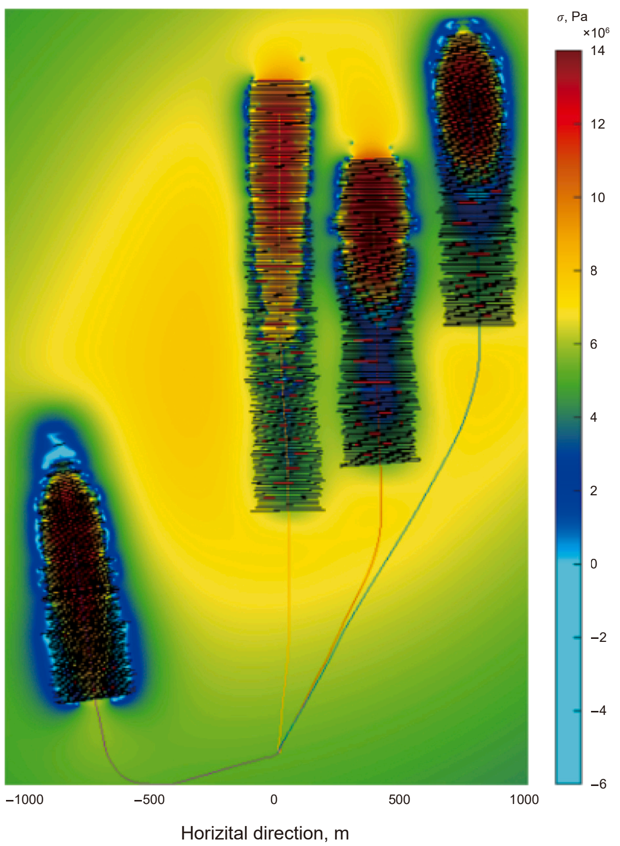

Fig. 18. Induced stress distribution at a depth of 3461.28 m in Fan Ye 1 well factory under S-SCP.

factory as an example, the leakoff coefficient near the wellbore can be calculated based on well logging data, as shown in Fig. 15.

The figure reveals that the leakoff coefficient fluctuates dramatically, indicating strong heterogeneity within the formation. In addition, the superimposed "stress shadow" effects between perforation clusters, fracturing stages, and different wells further hinder uniform fracture propagation—resulting in some zones receiving little to no effective stimulation. The S-SCP technique can mitigate inter-well and inter-stage stress interference, making it well suited for application in a well factory.

The S-SCP is applied in Fan Ye 1 well factory. The sweet spots in this well factory have an uneven spatial distribution. The inter-well spacing of the four test wells vary from 350 to 800 m (see Fig. 15). Both EXL and S-SCP use conventional zipper fracturing sequences, alternating back and forth from one end of the well factory to the other for fracturing. That is, from FY 1-4 well to FY 1-7 well, then from FY 1-7 well to FY 1-4 well, in a cycle, until the last operation stage of the well factory is completed. The lateral length of each well is 1800 m with 30 stages. Each stage is 60 m long; five perforation clusters are symmetrically distributed in each segment, with a cluster spacing of 12.5 m, and the clusters at both ends are 5 m away from the bridge plug. The injected fluid is slick water, with a viscosity of 0.003 Pa·s in 0.15 m^3/s rate. The total injection volume for each segment is 540 m^3.

Due to its significantly higher computational efficiency (by several orders of magnitude) compared to other numerical models, along with fully validated accuracy (Cheng, 2021; Cheng and Bunger, 2019a, 2019b; Cheng et al., 2016), we performed multi-parameter coupling optimization to determine the optimal perforation configuration. This optimization considered perforation numbers ranging from 5 to 12 holes per cluster and diameters varying between 6 and 10 mm, all adjusted according to spatially-dynamic stress conditions (Table 3 and Fig. 16).

With similar fracture growth in equal injection volumes, the S-SCP significantly reduces the energy consumption per unit fractured area compared to the EXL. Taking Well FY1-6 as an example, in the operation section from a measured depth of 4000 to 4238 m, the fracture scale of the S-SCP was weaker than that of the EXL, with a difference of about 10 m (see the gray area in Fig. 17). Despite this, the fracture length of the S-SCP was relatively more uniform within four consecutive stages, especially in the 24th and 25th stages, where the S-SCP had 15 m less variation in fracture length compared to EXL. The total fracture area and average energy consumption show that for Well FY1-4, the total fracture area of S-

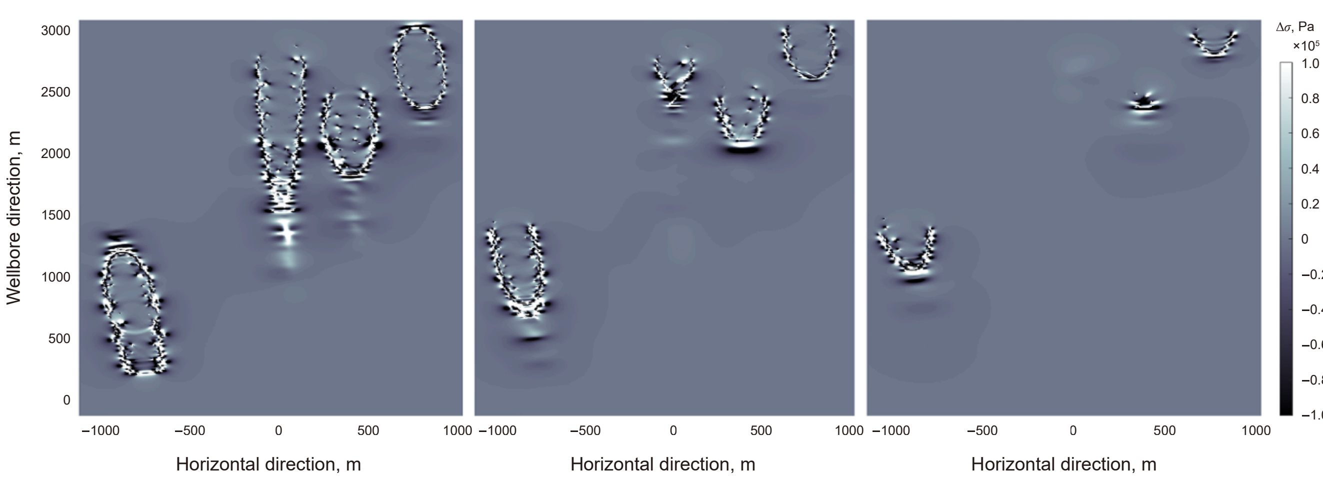

Fig. 19. Horizontal distribution of induced stress difference in Fan Ye 1 well factory using EXL and S-SCP.

SCP was 0.004% larger than that of EXL, meanwhile its energy consumption was reduced by 29%. This significant reduction in energy consumption with almost unchanged fracture area can also be observed in wells FY1-5, FY1-6, and FY1-7 (see Table 4).

The distribution of formation-induced stress by the S-SCP indicates that stress generated by deformation is highly concentrated near the toe of the well. This is because the closer the well trajectory is to the target point (depth is approximately −3460 m), the more horizontal the well trajectory becomes. The stress in the space is proportional to the distance from the center of the fracture. Therefore, at the horizontal slice depth for plotting, a compressive stress as high as 14 MPa appears on the toe side (Fig. 18). At the same time, the stress at the edge of the fracture is negative due to the tensile effect triggered by the initiation of the fracture at its end.

In order to more clearly demonstrate the impact of the two perforation techniques on stress distribution and also considering its' heterogeneity in three-dimension, a stress difference $\Delta\sigma$ section is displayed every 100 m starting from −3461.28 m. The values on this section are obtained by subtracting the stress induced by the EXL from the stress stimulated by the S-SCP.

Across all depths, it can be observed that the stress generated by the S-SCP is greater than that generated by the EXL (Fig. 19). This is due to the different mechanisms of how these two perforation techniques drive fracture expansion. The EXL controls the stress distribution of the fracture system through a substantial pressure drop, allowing the fractures to develop sufficiently under heterogeneous stress. In contrast, the S-SCP utilizes the elastic stress between fractures. By combining the tensile effect at the tip of the weakly developing fractures with the compressive effect on both sides of the superior fractures, it reduces the power needed to counteract the interaction stress (Eq. (13)). As a result, under the effect of the power balance Eq. (14), it encourages more fluid to be allocated from the main fracture to the un-developed ones, thus achieving a more evenly developed fractures at a lower energy cost. Therefore, on the stress difference section, the stress difference between EXL and S-SCP is greater near the edge of the fractures instead of the centre.

5. Conclusions

This study demonstrates that the proposed SCP technique significantly improves the efficiency of HF by optimizing perforation parameters in real time based on dynamic stress interference. Compared to the conventional EXL method, SCP achieves a more uniform fracture propagation and reduces energy consumption per unit fracture area by 22%–37%, while maintaining comparable total fracture area. The reported 22%–37% advantage is derived from a specific case study and therefore should not be regarded as universally representative. The actual magnitude of this benefit depends on the energy intensity of the particular EXL design employed, as well as on the operational strategy adopted for SCP fracturing. Fundamentally, SCP trades a slight reduction in fracture area for a substantial decrease in energy cost. The high computational efficiency of C5Frac is crucial for identifying and screening the optimization strategies that make this trade-off feasible. In addition, perforation erosion affects both EXL and SCP, but its impact is more pronounced for EXL because of its smaller initial perforation diameters. As erosion enlarges these perforations at different rates, the differences between EXL and SCP in both energy cost and fracturing performance tend to diminish over time. Further work will focus on real-time implementation and broader geological applications.

Most studies isolate elastic interference or entry-friction/flow partitioning, so they do not capture the closed-loop interaction among stress shadowing, flow competition, and near-wellbore effects. Our model addresses this gap by coupling these mechanisms; nevertheless, its semi-analytical framework—with simplified geometry and restricted physics—should be complemented by fully coupled numerical simulations to incorporate richer behaviours in the future.

CRediT authorship contribution statement

Cheng Cheng: Writing – original draft, Software, Methodology, Formal analysis, Conceptualization. **Gang Hui:** Writing – review & editing, Supervision, Methodology, Data curation. **Zhang-Xin Chen:** Writing – review & editing, Validation, Methodology, Investigation.

Declaration of competing interest

The authors declare that they have no known competing financial interests or personal relationships that could have appeared to influence the work reported in this paper.

Acknowledgments

This research has been made possible by contributions from the National Natural Science Foundation of China (52204029) and State Key Laboratory of Oil and Gas Reservoir Geology and Exploitation (No. CDUT-PLC2024006).

References

Abass, H.H., Soliman, M.Y., Tahini, A.M., et al., 2009. Oriented fracturing: A new technique to hydraulically fracture an open hole horizontal well. In: SPE Annual Technical Conference and Exhibition. https://doi.org/10.2118/124483-MS.

Baihly, J.D., Malpani, R., Edwards, C., et al., 2010. Unlocking the shale mystery: How lateral measurements and well placement impact completions and resultant production. In: SPE Tight Gas Completions Conference. https://doi.org/10.2118/138427-MS.

Bao, P., Hui, G., Hu, Y., et al., 2025. Comprehensive characterization of hydraulic fracture propagations and prevention of pre-existing fault failure in Duvernay shale reservoirs. Eng. Fail. Anal. 173, 109461. https://doi.org/10.1016/j.engfailanal.2025.109461.

Bunger, A.P., Lecampion, B., 2017. Four critical issues for successful hydraulic fracturing applications. Rock Mech. Eng. 5, 551–593. https://doi.org/10.1201/9781315364223-16.

Bunger, A.P., Peirce, A.P., 2014. Numerical simulation of simultaneous growth of multiple interacting hydraulic fractures from horizontal wells. Shale Energy Eng.: Tech. Chall. Environ. Issues Publ. Pol. 201–210. https://doi.org/10.1061/9780784413654.021.

Bunger, A.P., Jeffrey, R.G., Zhang, X., 2014. Constraints on simultaneous growth of hydraulic fractures from multiple perforation clusters in horizontal wells. SPE J. 19 (4), 608–620. https://doi.org/10.2118/163860-pa.

Chen, X., Zhao, J., Li, Y., et al., 2019. Numerical simulation of simultaneous hydraulic fracture growth within a rock layer: Implications for stimulation of low-permeability reservoirs. J. Geophys. Res. Solid Earth 124 (13), 227–249. https://doi.org/10.1029/2019jb017942.

Cheng, C., 2021. Stabilizing and enhancing energy efficiency for hydrocarbon stimulation considering subsurface uncertainty. Comput. Geotech. 140, 104433. https://doi.org/10.1016/j.compgeo.2021.104433.

Cheng, C., Bunger, A.P., 2016. Rapid simulation of multiple radially-growing HFs using an energy-based approach. Int. J. Numer. Anal. Methods GeoMech. 71, 281–282. https://doi.org/10.1002/nag.2471.

Cheng, C., Bunger, A.P., 2019a. Reduced order model for simultaneous growth of multiple closely-spaced radial hydraulic fractures. J. Comput. Phys. 376, 228–248. https://doi.org/10.1016/j.jcp.2018.09.004.

Cheng, C., Bunger, A.P., 2019b. Optimizing fluid viscosity for systems of multiple hydraulic fractures. AIChE J. 65 (5), e16564. https://doi.org/10.1002/aic.16564.

Cheng, C., Bunger, A.P., 2019c. Model-based evaluation of methods for maximizing efficiency and effectiveness of hydraulic fracture stimulation of horizontal wells. Geophys. Res. Lett. 46, 12870–12880. https://doi.org/10.1029/2019gl084809.

Cheng, C., Bunger, A.P., Peirce, A.P., 2016. Optimal perforation location and limited entry design for promoting simultaneous growth of multiple hydraulic fractures. Soc. Petrol. Eng. https://doi.org/10.2118/179158-ms.

Cipolla, C., Weng, X., Onda, H., et al., 2011. New algorithms and integrated workflow for tight gas and shale completions. In: SPE Annual Technology Conference and Exhibition. https://doi.org/10.2118/146872-MS.
Cornelius, L., Matthew, W., Mark, D.Z., 2018. Physics-based forecasting of man-made earthquake hazards in Oklahoma and Kansas. Nat. Commun. 9, 3946. https://doi.org/10.1038/s41467-018-06167-4.
Crouch, S.L., Starfield, A.M., 1983. Boundary Element Methods in Solid Mechanics. George Allen & Unwin, London. https://doi.org/10.1115/1.3167130, 50, 3, 704, 705.
Crump, J.B., Conway, M.W., 1988. Effects of perforation-entry friction on bottom-hole treating analysis. J. Petrol. Technol. 15474, 1041–1049. https://doi.org/10.2118/15474-PA.
Detournay, E., Cheng, A.H.D, 1993. Fundamentals of poroelasticity: Analysis and Design Methods, pp. 113–171. https://doi.org/10.1016/B978-0-08-040615-2.50011-3.
Dontsov, E.V., 2016. An approximate solution for a penny shaped hydraulic fracture that accounts for fracture toughness, fluid viscosity and leak-off. R. Soc. Open Sci. 3 (12), 160737.
Dontsov, E.V., Suarez-Rivera, R., 2020. Propagation of multiple hydraulic fractures in different regimes. Int. J. Rock Mech. Min. Sci. 128, 104270. https://doi.org/10.1016/j.ijrmms.2020.104270.
Dontsov, E., Hewson, C., Mark, M., 2023. Analysis of uniformity of proppant distribution between clusters based on a proppant-wellbore dynamics model. In: Paper Presented at the SPE/AAPG/SEG Unconventional Resources Technology Conference. https://doi.org/10.15530/urtec-2023-3854538.
Economides, M., Nolte, K.G., 2000. Reservoir stimulation. John Wiley & Sons, New York.
Ellsworth, W.L., 2013. Injection-induced earthquakes. Science 341, 142–149.
Entrekin, S., Trainor, A., Saiers, J., et al., 2018. Water stress from high-volume hydraulic fracturing potentially threatens aquatic biodiversity and ecosystem services in Arkansas, United States. Environ. Sci. Technol. 52 (4), 2349–2358. https://doi.org/10.1021/acs.est.7b03304.
Fisher, M., Wright, C., Davidson, B., et al., 2002. Integrating fracture mapping technologies to optimize stimulations in the Barnett shale. In: SPE Annual Technical Conference and Exhibition. https://doi.org/10.2118/77441-MS. San Antonio, Texas, SPE 77441.
Fisher, M.K., Heinze, J.R., Harris, C.D., et al., 2004. Optimizing horizontal completion techniques in the Barnett shale using microseismic fracture mapping. In: SPE Annual Technology Conference and Exhibition. https://doi.org/10.2118/90051-MS.
Howard, G.C., Fast, C.R., 1970. Hydraulic fracturing. Society of Petroleum Engineers, New York. https://doi.org/10.2118/2625-ms.
Huang, L., Liao, X., Fan, M., et al., 2024. Experimental and numerical simulation technique for hydraulic fracturing of shale formations. Adv. Geo-Energy Res. 13 (2), 83–88. https://doi.org/10.46690/ager.2024.08.02.
Hui, G., Chen, S., He, Y., 2021. Machine learning-based production forecast for shale gas in unconventional reservoirs via integration of geological and operational factors. J. Nat. Gas Sci. Eng. 94, 104045. https://doi.org/10.1016/j.jngse.2021.104045.
Hui, G., Chen, Z.X., Wang, H., et al., 2023a. A machine learning-based study of multifactor susceptibility and risk control of induced seismicity in unconventional reservoirs. Pet. Sci. 20 (4), 2232–2243. https://doi.org/10.1016/j.petsci.2023.02.003.
Hui, G., Chen, Z., Schultz, R., et al., 2023b. Intricate unconventional fracture networks provide fluid diffusion pathways to reactivate pre-existing faults in unconventional reservoirs. Energy 282, 128803. https://doi.org/10.1016/j.energy.2023.128803.
Hui, G., Chen, Z., Wang, Y., et al., 2023c. An integrated machine learning-based approach to identifying controlling factors of unconventional shale productivity. Energy 266, 126512. https://doi.org/10.1016/j.energy.2022.126512.
Hui, G., Chen, S., Gu, F., et al., 2024. Strike–slip fault reactivation triggered by hydraulic-natural fracture propagation during fracturing stimulations near Clark Lake, Alberta. Energy Fuel. 38 (19), 18547–18555. https://doi.org/10.1021/acs.energyfuels.4c02894.
Hui, G., Ren, Y., Bi, J., et al., 2025. Artificial intelligence applications and challenges in oil and gas exploration and development. Adv. Geo-Energy Res. 17 (3), 179–183. https://doi.org/10.46690/ager.2025.09.01.
Kondash, A.J., Lauer, N.E., Vengosh, A., 2018. The intensification of the water footprint of hydraulic fracturing. Sci. Adv. 4, 5982–5990. https://doi.org/10.1126/sciadv.aar5982.
Laurenzi, I.J., Jersey, G.R., 2013. Life cycle greenhouse gas emissions and freshwater consumption of Marcellus shale gas. Environ. Sci. Technol. 47 (9), 4896–4903. https://doi.org/10.1021/es305162w.
Lecampion, B., Desroches, J., 2015. Simultaneous initiation and growth of multiple radial hydraulic fractures from a horizontal well-bore. J. Mech. Phys. Solid. 82, 235–258. https://doi.org/10.1016/j.jmps.2015.05.010.
Long, G.B., Xu, G.S., 2017. The effects of perforation erosion on practical hydraulic-fracturing applications. SPE J. 22 (2), 645–659. https://doi.org/10.2118/185173-PA.
Meyer, B., Bazan, L., 2011. A discrete fracture network model for hydraulically induced fractures—theory, parametric and case studies. In: SPE Hydraulic Fracturing Technology Conference and Exhibition. https://doi.org/10.2118/140514-MS.
Miller, C., Waters, G., Rylander, E., 2011. Evaluation of production log data from horizontal wells drilled in organic shales. In: SPE North American Unconventional Gas Conference and Exhibition, pp. 14–16. https://doi.org/10.2118/144326-MS. The Woodlands, TX, USA, SPE 144326.
Mitchell, A.L., Small, M., Casman, E.A., 2013. Surface water withdrawals for Marcellus shale gas development: performance of alternative regulatory approaches in the Upper Ohio River Basin. Environ. Sci. Technol. 47 (22), 12669–12678. https://doi.org/10.1021/es403537z.
Peirce, A.P., Bunger, A.P., 2015. Interference fracturing: non-uniform distributions of perforation clusters that promote simultaneous growth of multiple HFs. SPE J. 20 (2), 384–395. https://doi.org/10.2118/172500-PA.
Peirce, A.P., Detournay, E., 2008. An implicit level set method for modeling hydraulically driven fractures. Comput. Methods Appl. Mech. Eng. 197 (33-40), 2858–2885.
Rice, J.R., 1968. In: Liebowitz, H. (Ed.), Fracture: an Advanced Treatise, 2. Academic Press, New York, pp. 191–311. https://doi.org/10.1016/b978-0-12-449704-7.50001-7. chap. 3.
Rijeka, C., 2016. Energy Information Administration. Trends in U.S. Oil and Natural Gas Upstream Costs. Intech.
Scanlon, B.R., Reedy, R.C., Nicot, J.P., 2014. Will water scarcity in semiarid regions limit hydraulic fracturing of shale plays? Environ. Res. Lett. 9 (12), 124011–124025. https://doi.org/10.1088/1748-9326/9/12/124011.
Sesetty, V., Ghassemi, A., 2013. Numerical simulation of sequential and simultaneous hydraulic fracturing. In: Bunger, A.P., McLennan, J., Jeffrey, R.G. (Eds.), Effective and Sustainable Hydraulic Fracturing, pp. 679–691. https://doi.org/10.5772/56309. Chap. 33.
Sneddon, I.N., 1951. In: Baker, B.B., Copson, E.T., Cumberlege, Geoffrey (Eds.), The Mathematical Theory of Huygens' Principle. Oxford University Press. https://doi.org/10.2307/3610572 vi, 192. The Mathematical Gazette, 35(311), 67.
Taghichian, A., Zaman, M., Devegowda, D., 2014. Stress shadow size and aperture of hydraulic fractures in unconventional shales. J. Petrol. Sci. Eng. 124. https://doi.org/10.1016/j.petrol.2014.09.034.
Vafi, K., Brandt, A., 2016. GHG frack: an open-source model for estimating greenhouse gas emissions from combustion of fuel during drilling and hydraulic fracturing. Environ. Sci. Technol. 50 (14), 7913–7920. https://doi.org/10.1021/acs.est.6b01940.
Vengosh, A., Jackson, R.B., Warner, N., et al., 2014. Critical review of the risks to water resources from unconventional shale gas development and hydraulic fracturing in the United States. Environ. Sci. Technol. 48 (15), 8334–8348. https://doi.org/10.1021/es405118y.
Wang, D.B., Qin, H., Wang, Y.L., et al., 2023. Experimental study of the temporary plugging capability of diverters to block hydraulic fractures in high-temperature geothermal reservoirs. Pet. Sci. 20 (6), 3687–3699. https://doi.org/10.1016/j.petsci.2023.07.002.
Wei, Z., Sheng, M., Li, J., et al., 2025. Pressure diagnostics in hydraulic fracturing for unconventional completion optimization. Adv. Geo-Energy Res. 17 (3), 196–211. https://doi.org/10.46690/ager.2025.09.03.
Weng, X., 1993. Fracture Initiation and Propagation from Deviated Wellbores. Society of Petroleum Engineers. https://doi.org/10.2118/26597-ms.
Wu, M., Chang, X., Guo, Y., et al., 2025. Advances, challenges, and opportunities for hydraulic fracturing of deep shale gas reservoirs. Adv. Geo-Energy Res. 15 (1), 1–4. https://doi.org/10.46690/ager.2025.01.01.